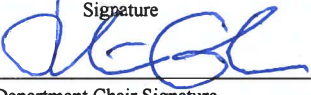**Leonardo van der Laat**

Magma fizz: tremor during the Kīlauea summit reservoir decompression

Submitted for Publication in:

Journal of Volcanology and Geothermal Research

in lieu of thesis in partial fulfillment of the requirements for the degree of
Master of Science in Earth and Environmental Sciences
Department of Earth and Environmental Sciences
The University of Michigan

Accepted by:

Zack Spica	Zack Spica	04/03/2023
Signature	Name	Date
	Yihe Huang	4/2/2023
Signature	Name	Date
	Julia Cole	8/15/23
Department Chair Signature	Name	Date

I hereby grant the University of Michigan, its heirs and assigns, the non-exclusive right to reproduce and distribute single copies of my thesis, in whole or in part, in any format. I represent and warrant to the University of Michigan that the thesis is an original work, does not infringe or violate any rights of others, and that I make these grants as the sole owner of the rights to my thesis. I understand that I will not receive royalties for any reproduction of this thesis.

☒ Permission granted.

☐ Permission granted to copy after: _____

☐ Permission declined.

Leonardo van der Laat
Author Signature

Earth and Environmental Sciences
M UNIVERSITY OF MICHIGAN

Magma fizz: tremor during the Kīlauea summit reservoir decompression

Leonardo van der Laat[a,*], Zack Spica[a], Corentin Caudron[b], Társilo Girona[c]

[a]*Department of Earth and Environmental Sciences, University of Michigan, Ann Arbor, Michigan, U.S.A.*
[b]*Laboratoire G-Time, Department of Geosciences, Environment and Society, Université Libre de Bruxelles, Brussels, Belgium*
[c]*Geophysical Institute, University of Alaska Fairbanks, Fairbanks, AK, USA*

Abstract

Typical eruptions at Kīlauea volcano involve the evacuation of magma from the summit reservoir towards the East Rift Zone. The reservoir drainage provokes the summit deflation, and in extreme occasions, such as in 2018, the summit caldera collapse. Systematically, summit deflation episodes have been accompanied by seismic tremor, often with a particular multichromatic spectral signature characterized by frequency gliding. In 2018, this type of continuous tremor accompanied the steady subsidence stage, whereas discrete earthquakes dominated the collapse stage. In this work, we seek to understand the source mechanism of the deflation-accompanying tremor of 2018. In order to locate the seismic source, we developed a novel machine-learning-based algorithm as an alternative to the amplitude source location technique. Provided with a large high-quality data set, our method outperforms the traditional technique, and therefore can potentially yield more accurate tremor locations. The tremor source was located 1 km below the eastern perimeter of the Halemaʻumaʻu crater, which coincides with the position of the summit magma reservoir, as determined in many other studies. Additionally, we detected infrasonic tremor, which originated at the summit active vent. Our analysis suggests that both seismic and infrasonic tremor sources were primordially driven by gas exsolution due to the decompression of the magma. We modeled the infrasonic source as a Helmholtz resonance generated in the void portion of the conduit due to the degassing at the atmospheric level. On the other hand, we modeled the seismic source as pressure oscillations driven by gas porous flow at the top of the reservoir. In this model, gas accumulates temporarily in many gas pockets between the magma and the roof. Each gas pocket, coupled with the rock immediately above it, acts as a single resonator generating one of the multiple spectral peaks. We inverted the tremor signal in order to estimate source parameters, namely, the gas mass flux rate and the thickness of the gas pockets. Our modeling shows that the gas flux was responsible for the tremor amplitude modulations, whereas the gas pocket thickness controlled the frequency variations. This source was periodically interrupted by the first small collapse events, generating a step-like pattern in amplitude and frequency gliding. Beyond a critical point of depressurization, the magma cannot contribute anymore to the tremor oscillations via decompression-driven degassing, neither support the roof above it, resulting in rock failure, i.e., earthquakes and collapse events. This work advances our understanding of magma-degassing dynamics and provides novel seismological techniques for volcano monitoring.

Keywords: tremor location, caldera collapse, subsidence, tremor inversion, frequency gliding, infrasound

Contents

---

[*]Corresponding author
Email address: `laat@umich.edu` (Leonardo van der Laat)

1. Introduction

1.1. Kīlauea volcano and summit deflation tremor

Kīlauea, in the Big Island of Hawai'i (Figure 1), is a widespread basaltic volcano with a plumbing system that is supplied with mantle-derived magma (Neal et al., 2019). Magma enters the shallow reservoir below the summit caldera, and then is distributed along the East Rift Zone (ERZ, Figure 1b). Typical eruptions at Kīlauea are characterized by summit deflation and magma extrusion at the ERZ, which suggests the evacuation of magma from the summit reservoir towards the east. Systematically, elevated seismic tremor has accompanied the summit deflation; for example in 1955 (Macdonald and Eaton, 1964), 1977 (Julian, 1994), 2007 (Poland et al., 2009; Unglert and Jellinek, 2015), 2011 (Supplementary Fig. S2) (Unglert and Jellinek, 2015), and 2018 (Soubestre et al., 2021). The duration of these tremor episodes is in the scale of days to weeks and they start immediately after the subsidence signal.

Understanding the processes that generate tremor is an important goal in physical volcanology, since this signal can be a useful precursor to eruptive activity. Although tremor has been successfully used to forecast eruptions (e.g., De la Cruz-Reyna and Reyes-Dávila, 2001; Dempsey et al., 2020; Ardid et al., 2022), current models are empirical and lack a theoretical physical basis. Thus, there is a need to understand the link between tremor and processes that trigger eruptions.

With no consensus, previous studies have proposed different models to explain the source of Kīlauea summit deflation tremor, such as: magma flow through constricted channels (Julian, 1994); driven oscillations of bubble clouds near the top of the shallow summit reservoir (Unglert and Jellinek, 2015); jerky motions of a cylindrical rock

2

piston (Soubestre et al., 2021); and resonance of a bubbly magma-filled crack (Soubestre et al., 2021). In this study, we seek to contribute to the understanding of the source of the Kīlauea summit deflation tremor, specifically during the 2018 eruption.

The 2018 eruption is of particular importance since the summit caldera collapsed due to the evacuation of magma from the summit reservoir (Anderson et al., 2019). In addition, a dike opened from the ERZ, specifically near the Puʻu ʻOʻō cone, where eruptions have occurred since the 1980's. This dike led further down east towards the Lower East Rift Zone (LERZ), resulting in a magma eruption located approximately 40 km east of the summit (Neal et al., 2019). This event is one of the few well-documented caldera-forming eruptions at a basaltic system, as the volcano benefits from one of the most comprehensive monitoring systems on Earth. Hence, this scenario represents a great opportunity to study seismoacoustic volcanic processes. In what follows, we focus on the processes taking place at the summit area.

1.2. Phases of the 2018 summit caldera collapse and associated seismicity

The 2018 collapse of the Kīlauea summit caldera can be understood as the succession of 5 distinct phases (Figure 2a). Phase 1 (April 1st - May 2) is the pre-collapse inflation stage, in which the lava lake attained its maximum elevation since it first appeared in 2008 (Supplementary Fig. S2a) and a rapid inflationary signal was detected (Patrick et al., 2020). Previous studies showed that summit deformation and the lava lake elevation are directly correlated (Patrick et al., 2015; Anderson and Poland, 2016), and that radial tilt is dominated by the reservoir pressure (Anderson et al., 2019). Additionally, weak tremor with frequencies between 0.4 and 1 Hz occurred during this phase (Figure 2b). This tremor lasted for years (Supplementary Fig. S1) and was driven by spattering activity at the lava surface (Patrick et al., 2016).

Phase 2 (May 2 - 17) was marked by the drainage of the lava lake and subsidence of the summit Figure 2b (Anderson et al., 2019). Three days after the magma evacuation started, an M6.9 detachment earthquake occurred at the volcano's south flank (Figure 1b, Figure 2b), and lava lake drainage and summit deflation accelerated immediately after (Anderson et al., 2019) (Figure 2b). During this phase, both infrasonic and seismic tremor were recorded (Figure 2b). In the past, infrasonic tremor at the Overlook vent (Figure 1) was associated with an increased degassing at the surface of the lava lake (Patrick et al., 2011; Fee et al., 2010). The seismic tremor after the M6.9 earthquake was strong and multichromatic, i.e., showed many prominent spectral peaks, with frequencies between 0.3 and 5 Hz (Figure 2c). Its amplitude was correlated to the deflation process: as radial tilt decreased almost linearly, tremor amplitude increased (Figure 2b). Tremor reached its maximum amplitude on May 14 when the deflation slowed down. The explosive activity at the Overlook vent started on May 10 and declined by the end of the month (Neal et al., 2019). During Phase 2, the explosion plumes reached ~2000 m above the summit (Neal et al., 2019). These explosions were probably triggered by the rock-fall impacts on the lava lake surface (Anderson et al., 2019), as previously documented by Orr et al. (2013).

Phase 3 (May 17 - 27) is defined by the first small collapse events. These events can be identified by the sudden increases in radial tilt (Anderson and Johanson, 2022) and decreases in tremor amplitude (Figure 2b). Although the overall multichromatic tremor amplitude decreased in Phase 3, its relationship with radial tilt is still inverse. In Phase 3, the explosive activity became more intense, with plumes reaching ~8100 m (Neal et al., 2019). In this case, the explosion trigger might have been rather related to the collapse of the rock overlying the magma reservoir (Neal et al., 2019).

In Phase 4 (May 27 - August 6), broad-scale collapse events started to occur, the explosive activity at the Overlook vent stopped, and the number of earthquakes increased. The earthquakes occurred in swarms of thousands of events between consecutive collapse events (Shelly and Thelen, 2019). The comparison of the relative seismic amplitude measurement (RSAM) and earthquake count curves in Figure 2a suggests that the seismicity during Phase 4 was dominated by earthquakes, with little or no tremor.

Phase 5, starting on August 6, is defined by the end of the eruption and the caldera collapse (Neal et al., 2019). The stabilization of the caldera is reflected by the sudden decrease in the number of earthquakes (Figure 2a). Also, RSAM dropped below the tremor background level recorded in Phase 1 (Figure 2a), which was associated with the spattering activity at the lava lake.

In this study, we focus on the seismic tremor recorded in Phases 2 and 3. Secondarily, we complement our investigation with the analysis of infrasonic tremor. For simplicity, we refer to seismic tremor simply as *tremor*, but for the infrasound signal, we use the *infrasonic* qualifying.
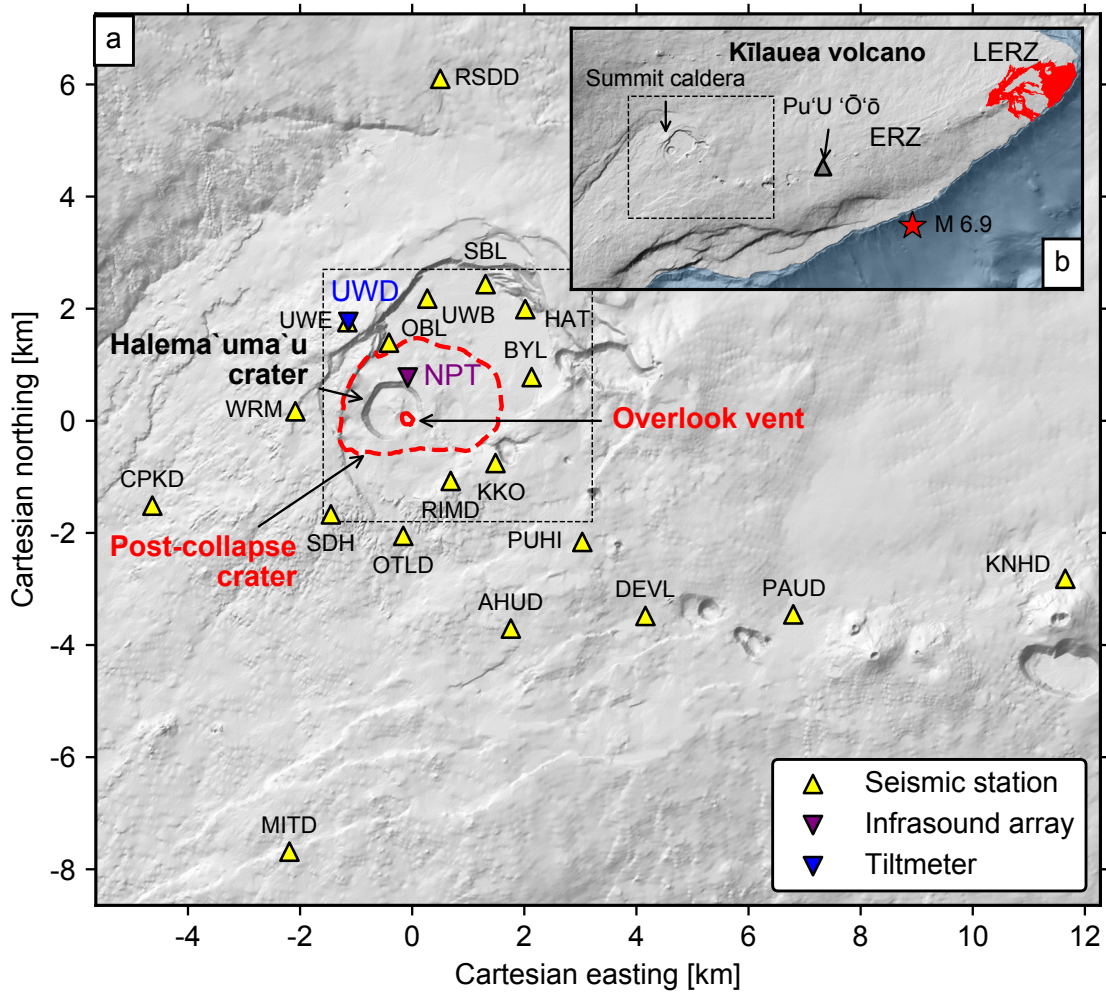
Figure 1: Map of Kīlauea volcano and the summit caldera. (a) Summit caldera area. Yellow triangles indicate seismic stations. CPKD, KNHD, MITD and OTLD were equipped with single vertical-component short-period sensors, AHUD and RSDD with three-component short period sensors and all other stations with three-component broad-band sensors. The blue inverted triangle is the UWD tiltmeter which is co-located with the UWE seismic station. The purple inverted triangle is the infrasound array NPT. The pre-collapse Overlook vent is shown with a red line. The red dashed line shows the post-collapse crater. The origin of the Cartesian coordinates corresponds to the position of the Overlook vent. The dashed rectangle shows the zoomed area in Figure 3 and Figure 5. (b) Main features of Kīlauea volcano: summit caldera, Pu'U 'Ō'ō cone, ERZ, and the LERZ, where the 2018 eruption took place (lava flows represented in red). The area of the map in (a) is represented by the dashed line rectangle. The red star indicates the M 6.9 detachment earthquake of May 4, 2018. The topography from U.S. Geological Survey (2017) is shown with a shaded relief.

1.3. Research questions

We revisit the tremor that accompanied summit deflation and explosive activity at Kīlauea volcano during the 2018 eruption, with a novel workflow to address the following questions: Where was the tremor source located beneath Kīlauea? What was the underlying process generating tremor? What changes in the source can explain the evolving characteristics of this type of tremor? Why did seismicity transition from continuous tremor to discrete events by the end of Phase 3? Since tremor and the explosive activity co-occurred in the same Phases 2 and 3, what was the connection between the two mechanisms, if any?

Since tremor exhibits emergent onsets and a long duration, classical arrival time techniques are unsuitable for source location. The tremor source location problem has been tackled for decades using small-aperture array methods
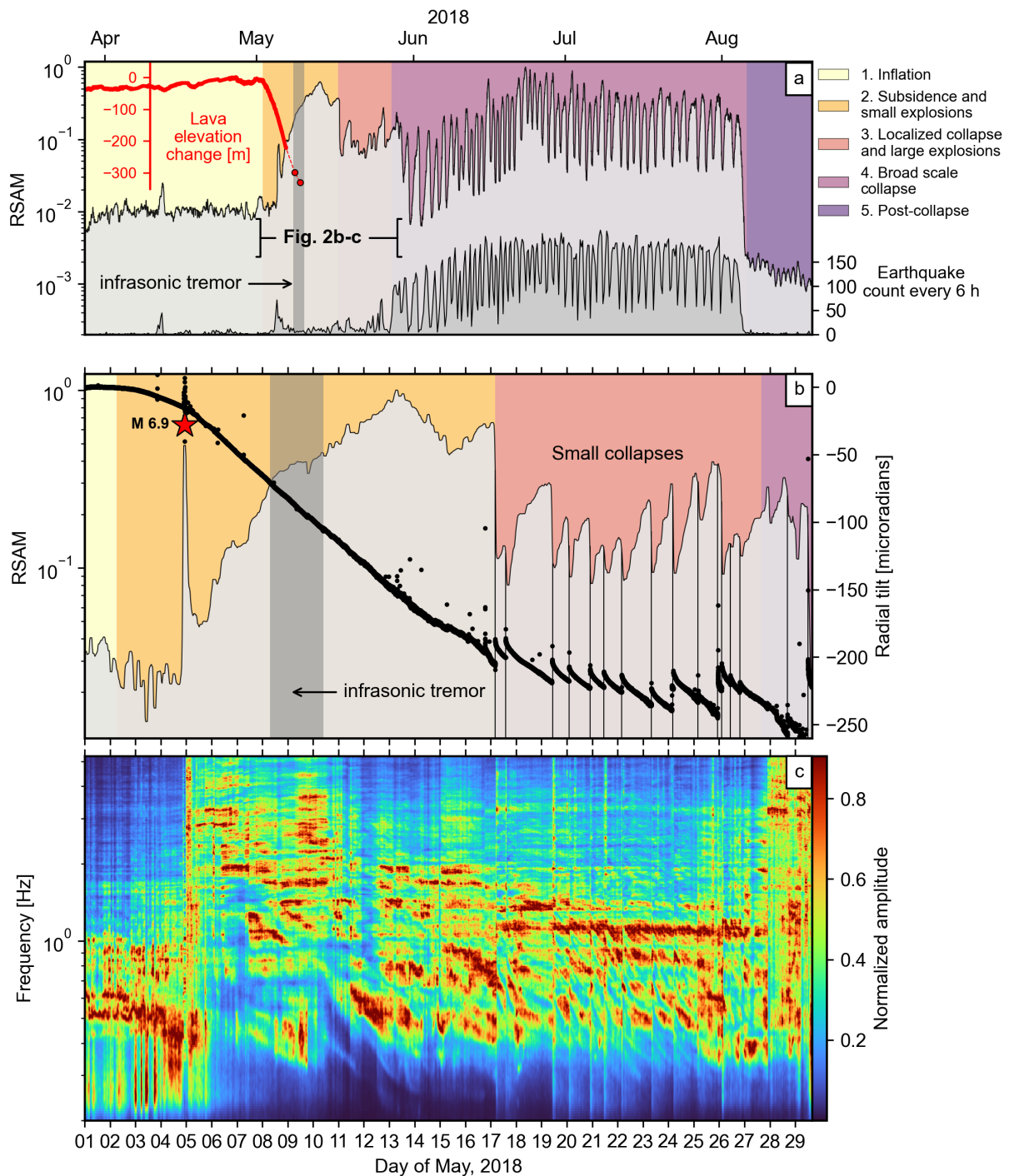
4

Figure 2: Seismicity and phases of the caldera collapse. (a) The RSAM for UWE vertical component, filtered between 0.5 and 10 Hz. was obtained , and computing root-mean-square amplitudes for 15-min moving window with 50% overlap. The RSAM curve was smoothed by taking the median on a 12-hour moving window. Earthquake count every 6 h from the USGS catalog. Lava lake elevation (Patrick et al., 2019) is shown in red. (b) Phases 2 and 3. The RSAM curve was smoothed with a shorter 4-hour moving window. Radial tilt data from the UWD are shown as black dots. The phases of the caldera collapse are represented with different colors in the background of plots (a) and (b). The M 6.9 detachment earthquake is indicated with a red star. The first small collapses are indicated with vertical lines. (c) Spectrogram for the vertical component of the UWE seismic station. The spectral amplitude was normalized with respect to the maximum amplitude at each 30-min long time frame. The gray vertical band in (a) and (b) represents the episode of infrasonic tremor.

5

(e.g., Almendros et al., 2001), amplitude decay techniques (e.g., Taisne et al., 2011; Ichihara and Matsumoto, 2017) or cross-correlation methods (e.g., Ballmer et al., 2013; Donaldson et al., 2017). In particular, Soubestre et al. (2021) located the Kīlauea summit tremor from the 2018 event using a cross-correlation method based on the first eigenvector of the network covariance matrix (Soubestre et al., 2019). In this method, the seismic amplitude information is disregarded since the signal is whitened during pre-processing (Seydoux et al., 2016). We propose to use the seismic amplitude information to locate this sequence of tremor. Instead of using the traditional amplitude source location (ASL) technique, we developed a novel machine-learning (ML) based method that takes advantage of the currently available wealth of data, i.e., event catalogs.

Our tremor location results and other observations suggest a source model for tremor from Phases 2 and 3. We propose that permeable gas flow due to magma decompression-driven degassing was the primordial cause of tremor. By performing tremor inversion, we estimate the source properties and provide numerical proof of the conceptual model using the mechanistic approach proposed by Girona et al. (2019). Additionally, we compare our results with independent modeling of gas exsolution due to reservoir decompression. To gain further insight into the degassing dynamics at the Kīlauea summit, we complement our analysis with the detection and modeling of infrasonic tremor.

2. Machine-Learning-based tremor location

Due to its lack of clear impulsive wave arrivals, volcanic tremor cannot be located using classical arrival time inversion techniques. Alternatively, researchers often solve this inverse problem using the ASL method. ASL is popular in volcanology and has been used in volcanic contexts to locate different types of events, especially those that produce a tremor-like continuous signal, such as: pyroclastic flows (e.g., Jolly et al., 2002), rock falls (e.g., Battaglia and Aki, 2003), eruption of basaltic material (e.g., Battaglia et al., 2005), lahars (e.g., Kumagai et al., 2009), migrations and ascents of magma (e.g., Taisne et al., 2011), convection cycles in lava lakes (e.g., Jones et al., 2006), and active lava fountains (Walsh et al., 2017).

The ASL method relies on the seismic attenuation model. In a homogeneous half-space, we can calculate the amplitude A_i^{calc} that is expected to be recorded at a station i, $i \in \{1, 2, \ldots, N\}$, and for a hypocentral distance d_i, with the function h:

$$A_i^{\text{calc}} = h(d_i) = S_i A_0 \frac{\exp{(-Bd_i)}}{d_i^{\alpha}}, \qquad B = \frac{\pi f}{cQ_f}; \tag{1}$$

where A_0 is the amplitude at the source, f is the frequency, c is the wave group velocity, Q_f is the quality factor of the medium of propagation, and S_i is the correction factor for site amplification effects. α is 1 for body waves and 0.5 for surface waves. The medium is simplified to a constant velocity half-space, and the radiation pattern of the waves is assumed to be isotropic.

In a 1-dimensional space, the inverse problem is solved by determining the estimate $\hat{d}_i$ that minimizes the objective function:

$$L = \|A_i^{\text{obs}} - h(\hat{d}_i)\|_2^2. \tag{2}$$

In our alternative ML approach, provided a set of n observed $(d_i^{\text{obs}}, A_i^{\text{obs}})$ pairs, obtained for discrete earthquakes, we estimate a function $\hat{h}$ that minimizes the objective function:

$$L = \|d_i^{\text{obs}} - \hat{h}(A_i^{\text{obs}})\|_2^2. \tag{3}$$

In this case, the estimated mapping function $\hat{h}$ does not depend on the attenuation model Equation 1, but it is derived directly from the data, i.e., an earthquake data set. Then, under the assumption that earthquake and tremor waves share similar amplitude decay functions, this map can predict the tremor location.

We propose that the $\hat{h}$ function can be estimated via feature engineering and linear regression, i.e.:

$$d_i^{\text{obs}} = \hat{h}(A_i^{\text{obs}}) = w_0 + \sum_{j}^{M} w_j \phi_j(A_i) + \epsilon; \tag{4}$$

where w_0 is the intercept or bias, w_j is the weight or coefficient for each j feature, which is obtained by transforming A_i with the ϕ_j function ($j \in \{1, 2, \ldots, M\}$), and ϵ is the misfit between the prediction and the observation. For one earthquake and many stations, using matrix notation, Equation 4 becomes:

$$\boldsymbol{d} = \boldsymbol{Xw} + \epsilon \tag{5}$$

where $\boldsymbol{d}$ is the vector of N hypocentral distances, $\boldsymbol{X}$ is a $N \times M + 1$ feature matrix, and $\boldsymbol{w}$ is the vector of $M + 1$ coefficients. As proof of concept, we first solved the 1-dimensional problem via ordinary least squares linear regression with both theoretical and real data (Supplementary Fig. S4). In the three-dimensional space, instead of solving for each hypocentral distance in the network, we obtain the absolute location of the earthquake:

$$\boldsymbol{Y} = \boldsymbol{XW} + \mathcal{E}; \tag{6}$$

where $\boldsymbol{Y}$ is the three-dimensional matrix with Cartesian coordinates of the earthquake hypocenter, $\boldsymbol{X}$ is the $N \times M + 1$ feature matrix, $\boldsymbol{W}$ is a $M + 1 \times 3$ matrix of coefficients, and $\mathcal{E}$ is the three-dimensional misfit.

Concisely, our ML-ASL method follows 3 fundamental steps: 1) feature extraction and engineering; 2) model training; and 3) prediction of new locations. Additionally, we performed synthetic tests in order to assess the uncertainties and limits of the model, as detailed in Appendix A and supplementary materials (Figs Sx).

During the Kīlauea summit caldera collapse, around 44,000 earthquakes were detected and located with high precision (Shelly and Thelen, 2019). This wealth of data represents an opportunity to explore the idea of solving the tremor location problem following an ML approach. When hypothesizing that tremor during Phases 2 and 3 originates under the Overlook vent at a depth of 1 km (Figure 1), the amplitude decay for tremor is very similar to that of the earthquakes of the catalog from Shelly and Thelen (2019) (Supplementary Fig. S3a & b), which supports our previous assumption.

3. Results

3.1. Feature extraction, engineering, and selection

The root mean square (RMS) amplitude values extracted from the earthquake records (20-s window from the origin time) show the expected exponential decay with respect to distance and magnitude (Supplementary Fig. S7). This is an important requisite to derive an ML model of amplitude decay. After training many models with all possible combinations of several transformations, we determined that the best-performing model was trained with the following features: the square root and the Lambert function of the amplitude ratios between all pairs of stations (Supplementary Fig. S8). This model was selected for tremor location and consisted of 9048 features.

3.2. Synthetic tests

As a proof of concept, we trained a model with synthetic amplitude data generated for the earthquake catalog using the theoretical attenuation law (Equation 1). After training, we relocated a reserved test set. The mean test error is 54 m. At this scale, the relocation data looks identical to the ground-truth values (Supplementary Fig. S9). This result demonstrates that, if the natural attenuation behaved in accord with the simple 1-layer model, our method would do an excellent job at relocating the events.

To determine the spatial limits of our model, we relocated every point in a 100-m spacing grid around the caldera, using the model trained with synthetic amplitudes. Then we computed the misfit between the predicted and the real locations (Supplementary Fig. S10). The distribution of the misfit depends on both the network configuration and the spatial extent and distribution of the earthquakes used for training. We observe that the misfits remain smaller than 500 m in the area of interest (dashed line rectangles in Supplementary Fig. S10). This means that, when relocating new events occurring in this area, if the attenuation was to behave according to the theoretical model, we could expect uncertainties smaller than this value.

3.3. Model performance

After training our model with real amplitude data, we relocated the reserved test set (30%) and the complete set. We computed the misfits for each Cartesian coordinate and the three-dimensional misfit, i.e., Euclidean distance between the real location and the predicted location. The distributions of the single coordinate misfits are centered around ~0 m (Supplementary Fig. S11), which indicates that there is no significant trend or bias in the model. The standard deviations are around 500 m for each coordinate. The mean test misfit error is 541 m, and the total misfit error is 494 m.

Additionally, we relocated the test set using the traditional ASL method in order to further assess the performance of our model. Both methods are able to relocate the seismicity in the expected general area of interest (Figure 3). Nevertheless, the results for the traditional ASL are widely dispersed (Figure 3b, e), whereas our ML-ASL method provides higher accuracy and precision (Figure 3c, f). With our alternative model, the structures of the seismicity are defined in much more detail than with the ASL method. The median misfit of the ML-ASL model (352 m) is almost three times smaller than the median misfit of the traditional ASL (1017 m).
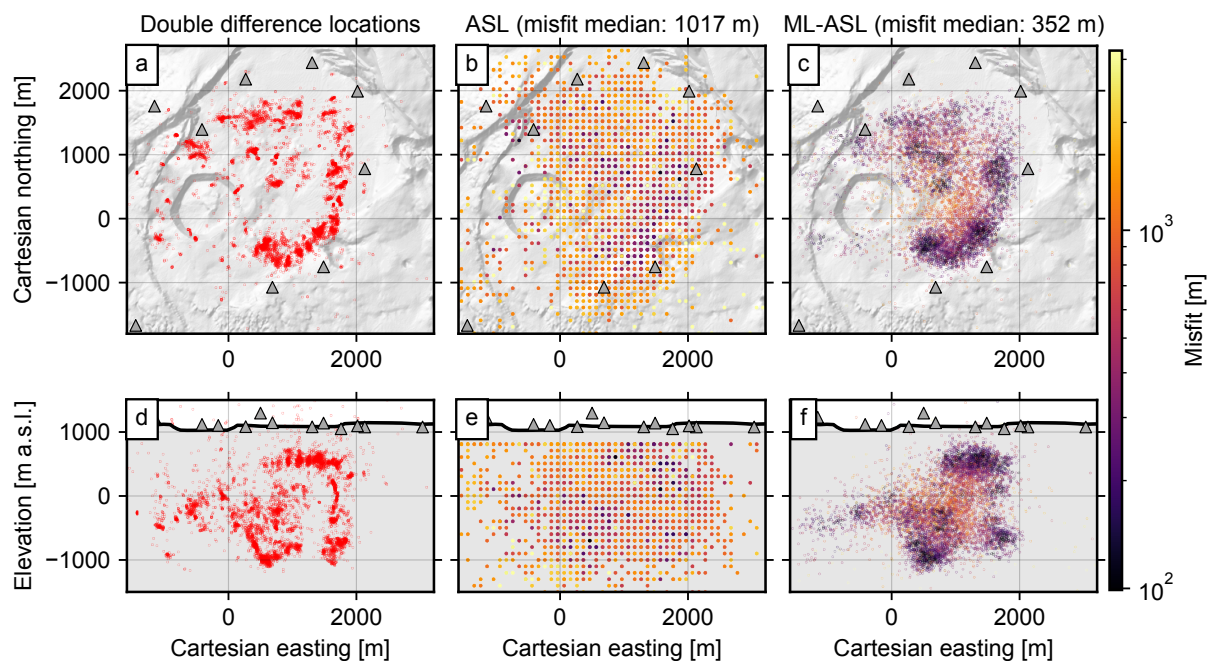

Figure 3: Comparison of classical amplitude source location (ASL) and machine-learning-based amplitude source location (ML-ASL) results. (a), (b) and (c): map view of the summit caldera; (d), (e) and (f): east-west profile section view. The left panel shows the test set portion (30%) of the earthquake catalog from Shelly and Thelen (2019). The center panel shows the ASL results. The right panel shows the results from ML-ASL method. In the center and right panels, the location of each event is color coded with respect to the misfit of each model. Seismic stations are represented as triangles. The dashed lines in the top panels indicate the Cartesian northing where the topographic profile at the bottom was taken. The topography from U.S. Geological Survey (2017) is shown with a shaded relief (top panels) and topographic profile sections (bottom panels). The origin of the horizontal Cartesian coordinates corresponds to the position of the Overlook vent.

3.4. Tremor location

We located tremor from Phases 2 and 3 using the ML-ASL method. For each phase, the amplitude and amplitude-ratio spatial distributions are consistent in time (Figure 4a, b). Sources from both phases are located around 1 km below the eastern perimeter of the Halemaʻumaʻu crater (Figure 5). The center of mass of the locations from Phase 3 is located slightly deeper and to the NW with respect to Phase 2 (Figure 5). The spread of the locations for Phase 2 is smaller than Phase 3. Phase 2 tremor has consistent locations trough time, whereas Phase 3 tremor has a larger spread in the data and some temporal fluctuations (Figure 4c, d, and e).
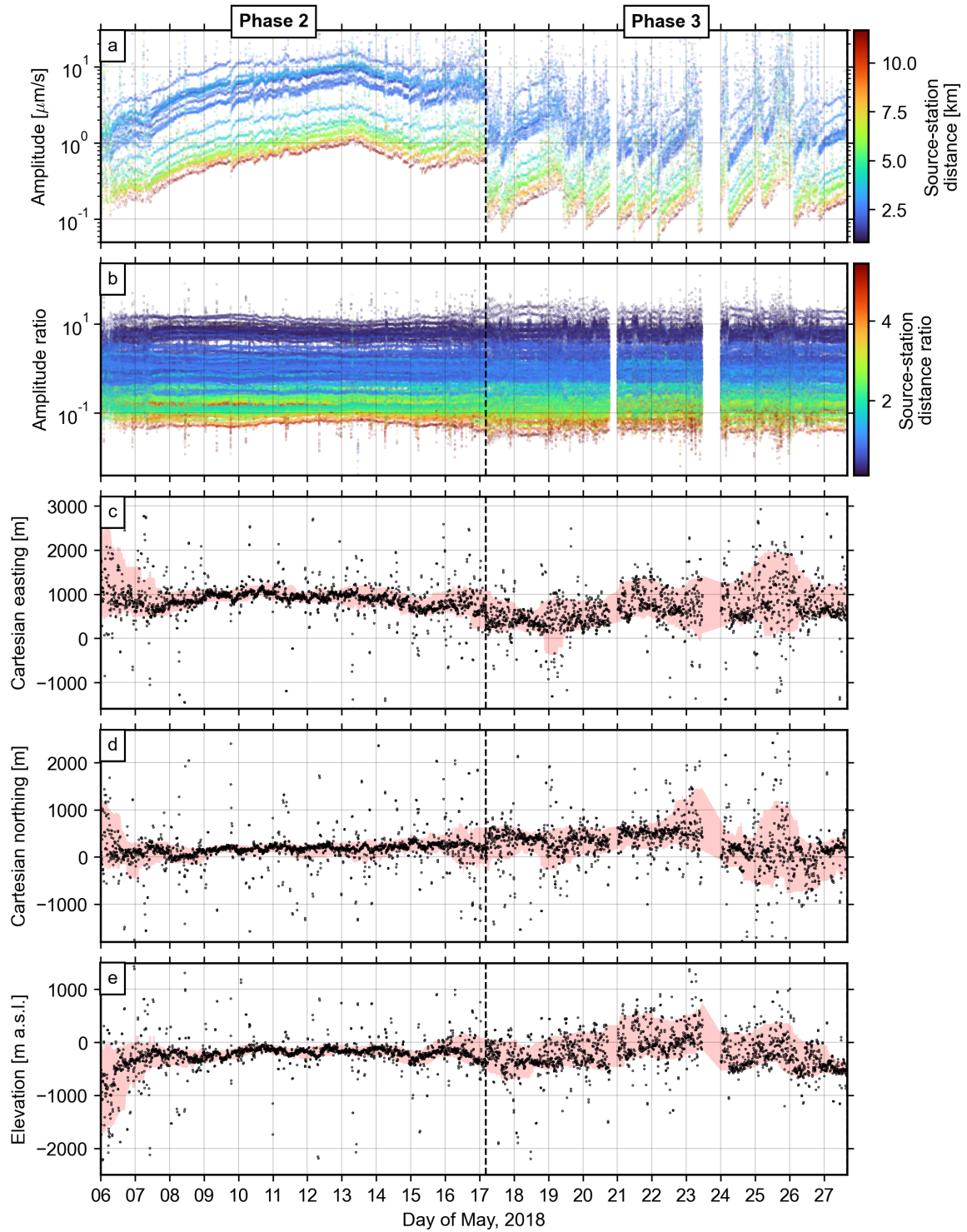
Figure 4: Tremor source location time series. (a): Seismic amplitude for each station. Each point is color coded with respect to the source-station distance as determined by our model. (b): Seismic amplitude ratios for each pair of stations. Each point is color coded with respect to the source-station distance ratio as determined by our model. (c), (d) and (e): Tremor source location, east, north, and vertical Cartesian coordinates, respectively. The pink area represents the range between the 10% and 90% quantiles in a 1-day moving window. The origin of the horizontal Cartesian coordinates corresponds to the position of the Overlook vent.

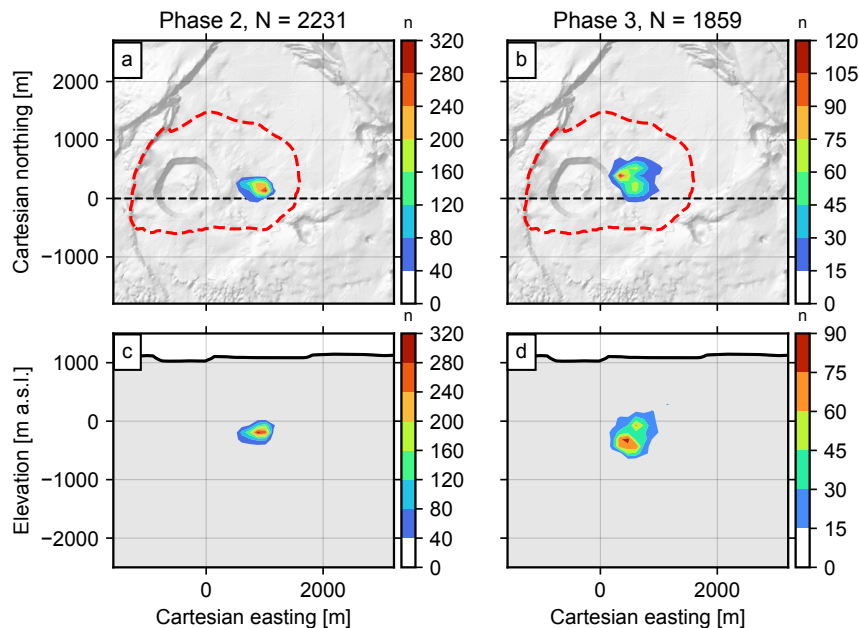Figure 5: Tremor source location results. (a) and (b): Map view of the summit caldera region. (d) and (e): West-east cross-section. In each panel, tremor source locations are shown as a two-dimensional histogram in the horizontal and vertical planes. The total number (N) of data points is indicated in the above the top panel. Triangles depict seismic stations. The dashed lines in the top panels indicate the Cartesian nothing, where the topographic profile at the bottom was taken. The topography from U.S. Geological Survey (2017) is shown with a shaded relief (top panels) and topographic profile sections (bottom panels). The origin of the horizontal Cartesian coordinates corresponds to the position of the Overlook vent.

The tremor from Phase 1, which originated at the surface due to the spattering activity of the lava lake in the Overlook vent, has very low amplitudes (Figure 2b). The intensity of this tremor is at the same level as the microseismic noise (Supplementary Fig. S5), and can be easily contaminated from foreign sources, especially the seismicity associated with the dike propagation at the ERZ (Supplementary Fig. S13) (Lengliné et al., 2021). The location of this tremor would require special treatment, and it is beyond the scope of this work. Instead, we refer to the analysis carried out by Patrick et al. (2016) and the location performed by Donaldson et al. (2017).

4. Discussion

In this section, we discuss the questions posed in Section 1.1. First, in Section 4.1, we compare our seismic tremor source location results with other geophysical studies carried out at the Kīlauea summit caldera area in order to understand the source position in the context of the magma plumbing system. Then, in Section 4.2, we discuss different models from previous studies for this type of tremor and provide a conceptual model based on our observations and analysis. In Section 4.3, we present our results for tremor modeling via inversion and independent magma decompression modeling in order to understand the properties of the source and its evolution. In Section 4.4, we address the potential connection between the tremor source and the explosions mechanism.

4.1. Tremor source located at the top of the magma reservoir

In this section, we put our tremor location results in the context of the current geophysical knowledge of the shallow structure and magma plumbing system at the Kīlauea summit. Several geodetic models unanimously point to a source of deformation, i.e., magma reservoir, whose center is located east of the Halemaʻumaʻu crater, at depths between 1.5 and 2.2 km (Poland et al., 2009; Baker and Amelung, 2012; Bagnardi et al., 2014; Anderson et al., 2019; Wang et al., 2021). Considering a radius of about 1 km for this source, our tremor source position coincides with the roof of the reservoir.

Using full-waveform inversion techniques, previous studies have located VLP events in a similar position as the one yielded by our tremor analysis, i.e., ~1 km below the eastern perimeter of the Halemaʻumaʻu crater (Chouet et al., 2010; Chouet and Dawson, 2013, 2011; Liang and Dunham, 2020; Liang et al., 2020). Although the underlying geophysical forward models used in those studies vary in their mechanisms and the involved geometries (e.g., dike system or spherical reservoir), there is consensus about the source position.

We compared the earthquake locations during the collapse stage (Shelly and Thelen, 2019) to our tremor locations results in Supplementary Movie S3. The tremor locations are tightly clustered inside the ring-like structure of the earthquakes. Although enclosed by earthquakes, the tremor source region occupies a space that is almost void of earthquake locations. In volcanic contexts, it is often thought that volcano-tectonic earthquakes occur at rock faults at the periphery of the magma (e.g. Roman and Cashman, 2006; White and McCausland, 2016). Thus, our observations suggest that, while earthquakes occurred at faults surrounding the reservoir in response to its decompression (Shelly and Thelen, 2019), tremor originated at the magma reservoir itself, specifically, at the top of the reservoir (Figure 6a).

4.2. Tremor model concept and previous studies

As introduced in Section 1.1, summit deflation processes at Kīlauea have been systematically accompanied by seismic tremor. Furthermore, this type of tremor shows a particular spectral signature. Some studies described it as *harmonic*, with dominant periods around 1 s (Macdonald and Eaton, 1964; Julian, 1994). Spectral analysis of recent events from 2007, 2011, and 2018 reveal a common multichromatic spectral signature characterized by slow (hours to days) frequency gliding (Unglert and Jellinek, 2015; Soubestre et al., 2021), as observed in Figure 2c. These characteristics can be perceived as a continuous fizzing sound with decreasing pitches, when reproducing the seismic records at human-audible frequencies; whereas earthquakes, such as the M 6.9 detachment event or the swarms of Phase 4, are heard as pop sounds (Supplementary Movie S1). The spectral peaks of this tremor are not evenly spaced (Figure 2b) and vary independently of each other in time and frequency. Thus, this signal cannot be classified as a typical *harmonic* tremor as observed in volcanoes such as Semeru (Schlindwein et al., 1995), Arenal (Lesage et al., 2006), and Turrialba (van der Laat et al., 2022), among many others. Accordingly, source mechanisms for these two distinct classes of tremor might be different. Therefore, for this case, we prefer the term *multichromatic*.

Previous studies have proposed diverse models to explain the mechanism generating tremor in this context. Macdonald and Eaton (1964) suggested that the summit tremor recorded in March 1955 was likely generated at moderate depth by the withdrawal of magma stored beneath the summit. Similarly, Julian (1994) proposed that the summit tremor episodes in March 1955 and September 1977 might be associated with magma flow as it evacuates the summit reservoir.

Based on spectral observations of the 2007 and 2011 events, Unglert and Jellinek (2015) attributed the origin of this tremor to evolving magma-bubble dynamics, such as driven oscillations of bubble clouds near the top of the shallow summit reservoir (~1 km deep). The authors associated the frequency gliding with changes in the geometry of the bubble cloud in response to the magma flow.

In 2018, tremor accompanied the steady subsidence (Phase 2) and the first small collapse events (Phase 3). Both phases share similar tremor characteristics: 1. amplitude increase in correlation to the decompression (inverse tilt, Figure 2b); and 2. multichromatic downward frequency gliding (Figure 2c). The most important difference between the two signals is that the amplitude increase and the frequency gliding in Phase 3 were interrupted by the collapses. Thus, we can think of two possible scenarios: 1. both phases of tremor share a common source that was periodically interrupted by the collapse events in Phase 3; or 2. two different sources for each phase.

Based on tremor location and spectral analysis, Soubestre et al. (2021) favored a scenario with two different sources. For Phase 2, the authors proposed that the observed signal corresponds to swarms of periodic earthquakes induced by the jerky motions (stick-slip) of a cylindrical rock piston progressively intruding into the depleting shallow hydrothermal system. The succession of earthquakes would act according to the Dirac comb effect, in which the frequencies f_n of the resulting tremor spectral peaks are integer multiples of the inverse of the recurrence period τ, i.e., $f_n = n/\tau$. In their modeling, the authors arbitrarily limited the number of inverted frequencies so that they were all related to the same τ at each time frame (e.g., for $\tau = 2.22$, $f_1 = 0.45$ Hz, $f_2 = 0.9$ Hz and $f_3 = 1.35$ Hz; Figure 9 in Soubestre et al. (2021)), while disregarding other prominent peaks that do not fit this model. Nevertheless, it is clear that, even if this tremor is multichromatic in nature, these peaks are not evenly spaced and do not glide in concert (Figure 2c). In addition, the increasing amplitude trend of this tremor (Figure 2b) was not addressed by the authors.
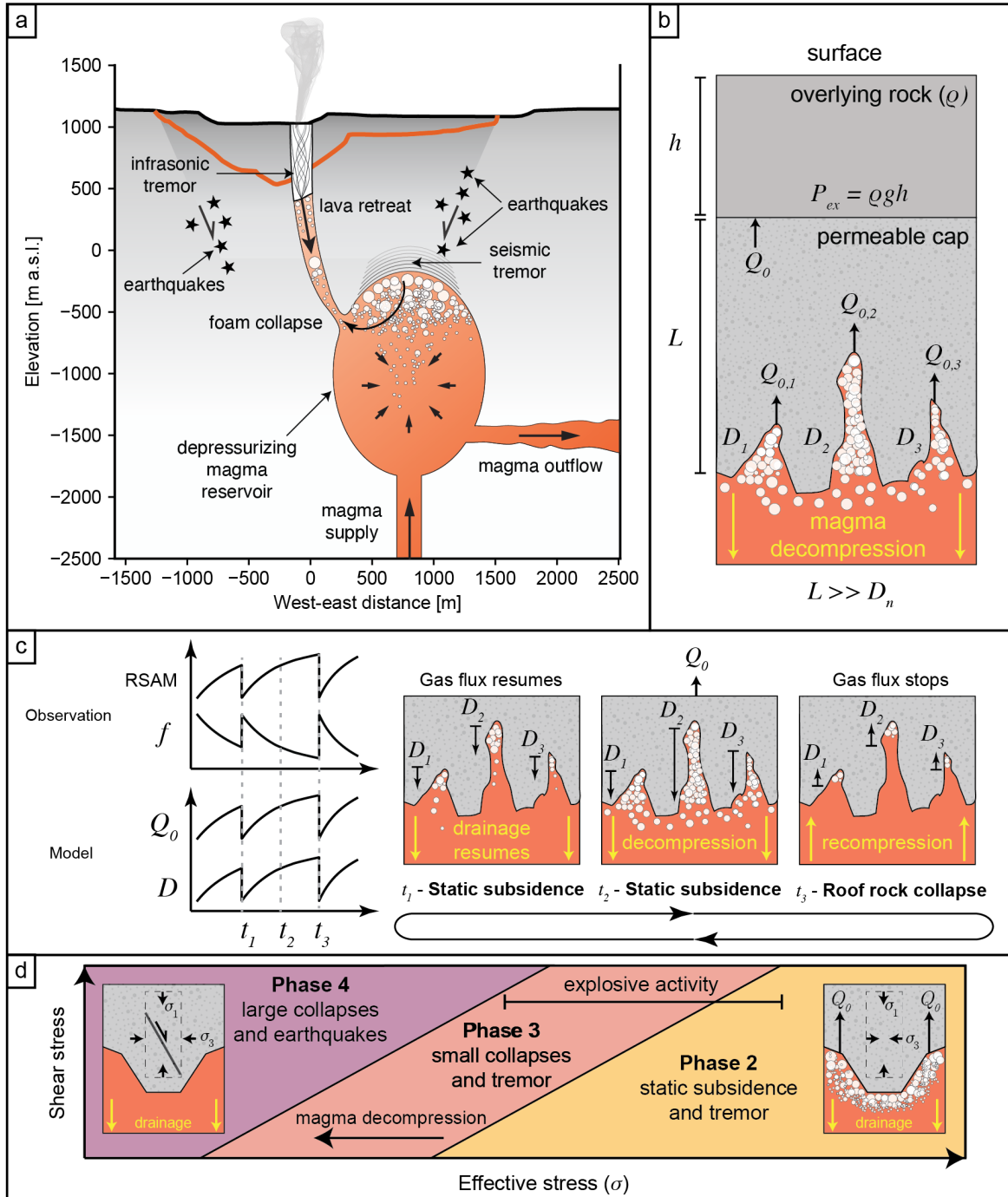
Figure 6: Conceptual interpretation model. (a) West-east cross-section of the Kilauea summit caldera and the source of tremor. The thick black and red lines show the topography east-west profile before and after the collapse, respectively. (b) Conceptual model for tremor source of Phases 2 and 3. h is depth of the upper boundary of the resonator. ρ is the mean density of the rock above the resonator. P_{ex} is the external pressure at depth h. L is the thickness of the permeable cap. Q_0 is the total gas flux rate, which is the sum of the fluxes $Q_{0,n}$ for n resonators. D_1-D_3 are the thicknesses of different gas pockets. (c) Cycles of tremor during Phase 3. Tremor fluctuations amplitude (RSAM) and frequency (f), are explained by changes in Q_0 and D under the influence of the collapse events. (d) Conceptual Mohr-Coulomb stresses diagram that illustrates the transition between seismicity regimes. The colors for Phases 2-4 are the same as in Figure 2a and b. σ_1 and σ_3 are the maximum and minimum principal stresses, respectively.

12

In their model, between May 7 and 14: (1) the slip distance decreases between the start and the end of Phase 2, from 0.09 mm to 0.05 mm; (2) the velocity of the earthquakes decreases from ∼0.12 mm/s to ∼0.07 mm/s; and (3) the recurrence time τ increases from 1.02 s to 4.06 s. From such a model, it is unclear how the amplitude of the resulting tremor would decrease, instead of increasing as observed (Figure 2b).

For Phase 3, Soubestre et al. (2021) proposed a different model. The authors suggest that tremor originated due to collapse-triggered resonances of a bubbly magma-filled crack (Chouet, 1986). In their model, the progressive amplitude increase after each collapse (Figure 2b) was not addressed. If the collapses were triggering the resonances, it would be expected that the amplitude decreased after the excitation, contrary to what is observed (Figure 2b). In this model, the frequency gliding is explained by changes in the gas volume fraction in the crack. Each collapse would have the effect of recompressing the magma, and forcing the gas back into the melt, gradually decreasing the gas fraction. In turn, this evolution of the gas fraction would have been responsible for the decrease in the resonance frequencies. In order to explain the sudden increase in frequency with each collapse, the authors recur to a systematic increase in the mode of resonance. While the authors suggest that the excitation of different modes might be related to the differences in the location of the collapses, the incremental character of the mode evolution remains unclear.

Based on our location results, the volcanic context, and the recent discussion, we favor a scenario in which both phases of tremor correspond to the same source, which was periodically interrupted by the collapses in Phase 3. The correlation between the decompression (inverse tilt) and the tremor amplitude (Figure 2b), suggests that the primordial cause of tremor was volatile exsolution caused by decompression of the summit magma reservoir (Johnson, 1992; Poland et al., 2009; Unglert and Jellinek, 2015). Our location results point to a source near the roof of the reservoir, as discussed in Section 4.1. Thus, we propose that the exsolved gas temporarily accumulated in this region, forming a layer of foam (Jaupart and Vergniolle, 1989) (Figure 6a). Then, gas from this layer would have flowed through the permeable rock of the reservoir roof, generating pressure oscillations observed as tremor (Girona et al., 2019).

This mechanism of tremor generation would have vanished by the end of Phase 3, as we observe a transition from a tremor-dominated to an earthquake-dominated regime (Figure 2a). This observation can be understood from the Mohr-Coloumb stresses point of view (Figure 6d). As the magma evacuates and decompresses, the effective stress on the overlying rock decreases, while the gas exsolution triggers tremor. This process continues until the magma becomes relaxed enough to stop supporting the rock, and to decrease the vigor of the exsolution (cessation of tremor). At this critical pressure (Anderson et al., 2019), the shear stress in the rock is sufficiently high to cause rock failure, which is reflected by discrete earthquakes and large collapse VLP events.

In order to support our conceptual model for the tremor source, we inverted the tremor signal using the forward model from Girona et al. (2019) as discussed in the following Section 4.3.

4.3. Tremor inversion

We invert tremor from Phases 2 and 3 following Girona et al. (2019), assuming that tremor is generated by pressure oscillations beneath a permeable cap. The oscillations are the result of three concurrent processes: (1) the random supply of volatiles; (2) the temporary accumulation of a gas pocket beneath the cap; and (3) the porous flow of gases through the permeable cap (Figure 6b). The resonator, consisting of the gas pocket and the cap, has a natural frequency of resonance f_{nat}.

Girona et al. (2019) showed that if the gas pocket thickness D is lower than a critical value D_{crit}, the amplitude spectrum is monochromatic; i.e., it shows a peak corresponding to f_{nat}. Conversely, if $D > D_{crit}$, the pressure amplitude spectrum follows a power law distribution. In our case, the observed tremor shows multiple spectral peaks that are independent of each other in time and frequency (Figure 2c). Thus, we consider that each peak is generated by a single resonator (Figure 6b). The resulting signal is the sum of many concurrent pressure oscillations. In our inversion, we limit the number of resonators that could contribute to the generated synthetic tremor, based on the number of the most prominent spectral peaks observed in the tremor signal.

Several scenarios for a system of resonators could be proposed. In the scenario that we favor, the gas pockets could be at a similar depth situated between the magma and the reservoir roof, as depicted in Figure 6b, but accumulate in pockets of different thicknesses due to the irregularities of the roof surface and/or the differences in the degassing rate across the reservoir.

We performed a non-sequential inversion, i.e., each time frame was inverted independently, using the genetic algorithm. In order to decrease the parameter space, we fixed the parameters that are not expected to vary significantly

in time, such as the source position, the properties of the gas, the properties of the permeable cap, and the properties of the medium of propagation. Instead, we invert for the source parameters that are expected to vary the most and modulate the tremor amplitude and spectral characteristics (Girona et al., 2019): gas flux rate $Q_{0,n}$ and the gas pockets thickness D_n for each resonator n.

In order to constrain the fixed parameters, we conducted a parametric analysis. A detailed explanation of the tremor inversion and parametric analysis can be found in Appendix B. The values of the parameters used for the final inversion can be consulted in Table B.1. To estimate the uncertainty of our model, we repeated the experiment 1000 times. We report mean values for the estimated parameters and the range between the 5% and 95% percentiles.

Our models can reproduce the most prominent spectral features and amplitude variations (Figure 7). Each n resonator has a different gas mass flux $Q_{0,n}$ at any given point. We observe an inverse relationship between $Q_{0,n}$ and f_{nat} (Supplementary Fig. S18). The total values of Q_0 fluctuate between a few kg/s up to 700 kg/s. The interval of confidence of our estimation is smaller than the temporal variations, and ~11% of the median estimate (Supplementary Fig. S17). The estimated Q_0 follows a similar trend as the seismic amplitude (Figure 8b), with the exception of the time period between May 9 and May 11, where we observe a decrease in the flux rate. This coincides with the disappearance of the lower frequency peak (< 1 Hz) on May 9 (Figure 7a & b).

We also compared the estimated gas flux from the tremor inversion with an independent model based on the decompression of the magma reservoir (Figure 8b). Given a reservoir decompression sequence, and a starting magma composition, we can model the degassing history, i.e., a series of volatile concentrations in the liquid and fluid that a magma will follow during decompression (Dixon, 1997). As Anderson et al. (2019) showed, the summit radial tilt is a proxy of the reservoir pressure. We used the relationship established by the authors to estimate the pressure of the reservoir (Figure 8a), and based on that, we modeled the degassing path. We only considered the steady subsidence in Phase 2, since the collapses in Phase 3 re-compressed the reservoir. A detailed explanation of our modeling can be found in Appendix C. For comparison with our tremor model Q_0 estimate, we refer to the decompression-derived flux rate as Q^D.

Both models for the gas flux show a similar range of values. Nevertheless, before May 13, Q_0 is smaller than Q^D. Also, since tremor started four days after the decompression, there is a corresponding delay between the two estimates. However, by May 13, Q_0 reached similar values (~700 kg/s) as Q^D. Also, the decrease and increase that occurred between May 14 and 17, match in both models, although with a slight delay for the tremor model.

The difference between the two mass flux estimates indicates that some degassing is not accounted for by the tremor model. This could correspond to passive degassing, in particular, through the conduit out to the surface. The detected infrasonic tremor is evidence of this degassing in the vent (Fee et al., 2010). On the other hand, the delay between the two estimates may reflect the time interval between the exsolution and tremor generation. This time interval must take into account the rising time of the bubbles in the magma and the residence time of the gas in the foam layer before the transmission through the permeable cap.

The estimated values for the gas pocket thickness D are between around ~0.5 mm to up to a ~20 cm (Figure 9). The interval of confidence of our estimation is smaller than the temporal variations and ~5% of the median estimate (Supplementary Fig. S17). We observe an inverse relationship between the frequency of the spectral peak and the gas pocket thickness D. The observed downward frequency gliding is explained by the increase in the gas pocket thickness (Figure 9). We observe some linear clusters of increasing D, both during Phases 2 and 3.

This model explains both cycles of tremor amplitude and frequency gliding. The tremor amplitude cycles during Phase 3 are explained by Q_0 variations (Figure 8b). We interpret that with each collapse event, the magma is suddenly recompressed, which causes the exsolution to stop (t_3 in Figure 6c). After each collapse, the evacuation and decompression process continues, allowing for the gradual gas exsolution and tremor generation (t_1 and $_2$ in Figure 6c). On the other hand, the cyclic downward frequency gliding is explained by the expansion of the gas pockets, which, with each collapse can be recompressed (Figure 6c) or ascend through the conduit and contribute to the explosions. Our modeling is consistent with interpretations from Shelly and Thelen (2019) and Hotovec-Ellis et al. (2022), who attributed their observations, i.e., cyclic swarms of earthquakes and oscillations of seismic velocity, respectively, to the gradual decompression of the reservoir, followed by a sudden recompression caused by a collapse event. In the next section, we discuss the implications that this model could have for explosive activity. In particular, the plausibility of generating explosions via foam collapse as suggested by Jaupart and Vergniolle (1989).
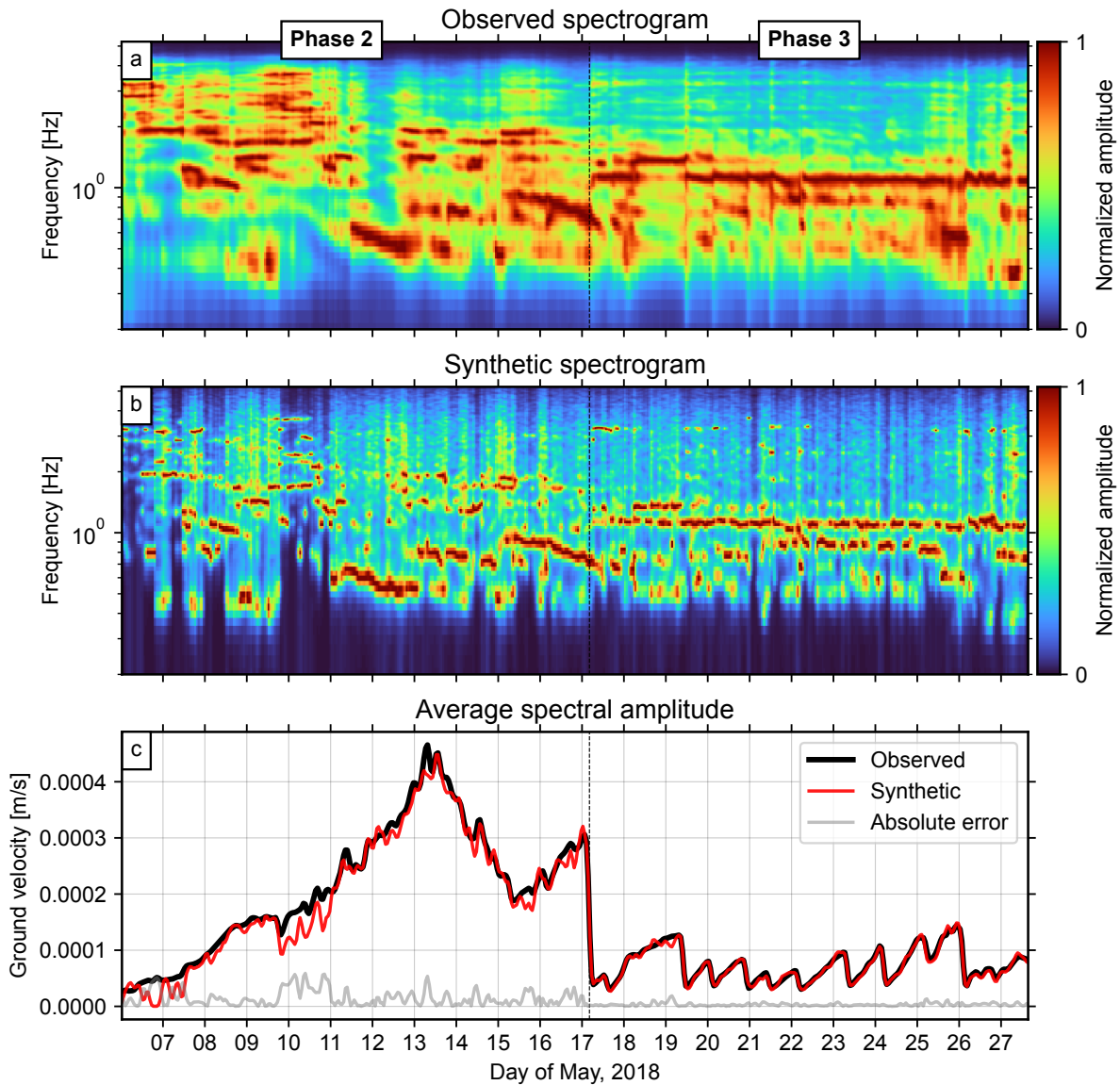
14

Figure 7: Observed and simulated tremor for Phases 2 and 3 at station UWE. (a): Observed spectrogram. (b): Synthetic spectrogram for the best-fit model. The spectrograms are normalized with respect to the maximum amplitude within each frame. (c): Average spectral amplitude for the observed (black line) and synthetic data (red line).

4.4. Connection between tremor and explosive activity

We approach the co-occurrence of tremor and explosive activity in Phases 2 and 3, and discuss the potential connection between the two involved mechanisms. As expected from the model of Jaupart and Vergniolle (1989), if the foam layer at the top of the reservoir grows too large it collapses into a large gas pocket which rises through the conduit, and generates an explosion at the surface. In this section, we discuss the plausibility of this type of "bottom-up" process taking place during the 2018 event.

The explosion on May 9, which terminated the thermal camera's image stream (Supplementary Movie S2), occurred at the same time as the tremor's lowest frequency peak stopped (0.5 Hz, Figure 2c and Supplementary Fig. S22). On the contrary, higher frequency peaks (1-5 Hz) continued after the explosion. These observations could be interpreted following (Jaupart and Vergniolle, 1989). The explosion on May 9, could be due to the collapse of the
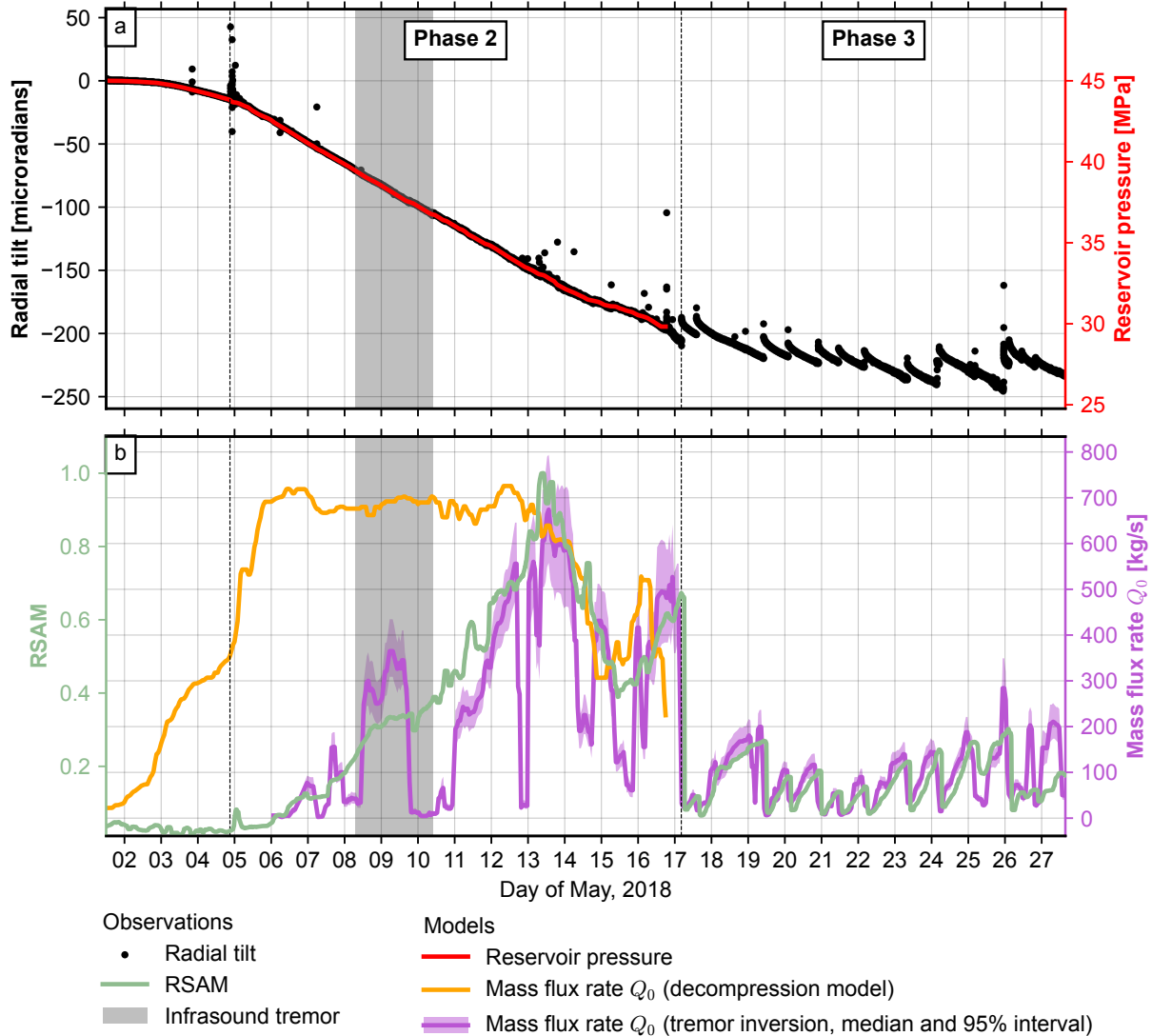
15

Figure 8: Gas flux rate models. (a) Radial tilt (black dots) at UWD and tilt-derived magma reservoir pressure model Anderson et al. (2019) (red line). (b) Normalized RSAM (green line) and gas flux models. For the gas flux derived from the decompression model (orange line), we use a starting magma composition of 0.3 wt% H_2O and 0.65 wt% CO_2 (Gerlach and Graeber, 1985), a density of 2650 kg/m^3 and a reservoir volume 3.6 km^3, as estimated by Anderson et al. (2019). The gas flux derived from the tremor inversion for station UWE. The tremor experiment was repeated 1000 times; we show the median and 95% confidence interval of the results.

largest gas pocket associated with the tremor's lowest frequency peak. According to our results, this gas pocket had a thickness at a depth of ~15 cm (Figure 9). This could have been the critical thickness at which the foam collapses, which, for a basaltic reservoir, can vary between 4 cm and 40 m (Jaupart and Vergniolle, 1989). Since the other gas pockets had smaller thicknesses, they would have persisted independently.

The seismic signal associated with the explosion is composed of two phases: a first low-amplitude, short-period (SP) phase is followed by a very-long-period (VLP) phase of high amplitude (Supplementary Fig. S23). In the infrasonic signal, only the VLP phase is present. Considering the collapsing foam model, the first SP phase in the seismic records could be associated with the foam collapse and its ascent through the pipe, whereas the VLP phase could be associated with the explosion at the surface of the lava column. Nevertheless, the delay between the SP and the VLP phases is too short ($\Delta t \approx 13$ s) to account for the travel time through a long pipe. According to Vergniolle
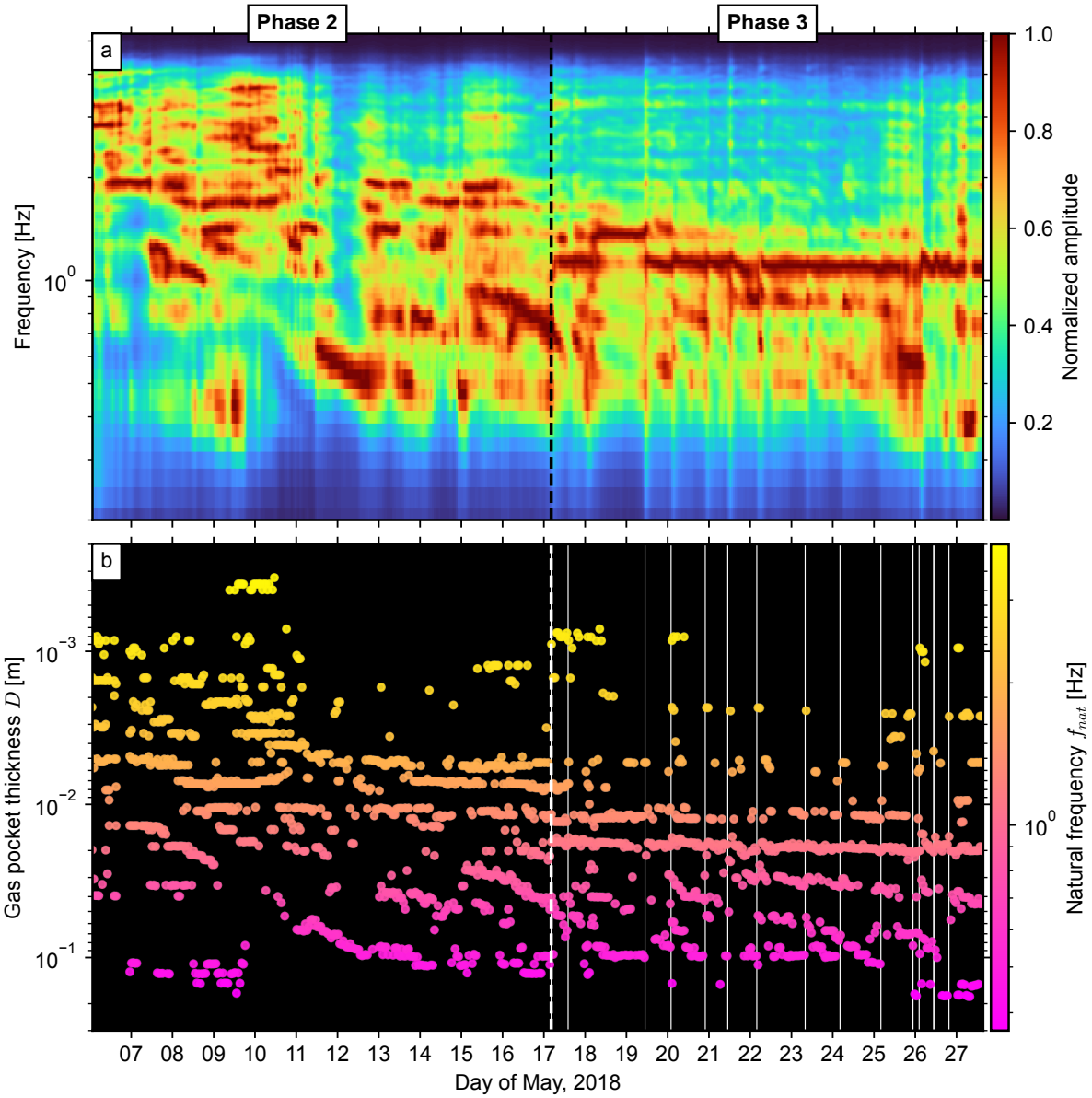
Figure 9: Gas pocket thickness estimates from the tremor inversion for station UWE. (a): Spectrogram for station UWE (b): Gas pocket thickness. Each point corresponds to an individual resonator at a given time frame. The dots are color-coded with respect to the natural frequency of the resonator. Note that the vertical axis (b) is inverted in order to highlight the inverse relationship between the gas pocket thickness and the natural frequency of the resonator. The thin vertical lines (b) represent the collapse events. The 95% confidence interval derived from 1000 experiments is too small to be represented in this figure, around 5% of the median value (Supplementary Fig. S17).

and Jaupart (1990), the ascent velocity v_s of a gas slug is given by $v_s = 0.345\sqrt{gD}$, where D is the diameter of the conduit. For realistic values of D between 100 and 300 m, $v_s \approx 11\text{-}18$ m/s, and with $\Delta t \approx 13$ s, the height of the pipe would be ~140-240 m. This height would be more than three times smaller than the one that is derived from our tremor location and the lava lake elevation measurements (~750 m).

Another more likely possibility is that this explosion was not triggered at depth, but at the surface by a rock-fall on the lava surface. This type of process was observed during the explosion of May 4, 2018 at 21:00 (Supplementary

17

Movie S2), and was thoroughly documented by Orr et al. (2013) for the Kīlauea eruption of 2011. For that eruption, the authors reported a similar composite seismic signal for hundreds of rock-fall/explosion events. The SP phase was coincident with the main body of rock striking the lava lake surface, whereas the ash emission and outgassing that followed this impact corresponded to the onset of the VLP phase (Orr et al., 2013). The sudden disappearance of the tremor's lowest frequency peak after the explosion can be explained with a "top-down" mechanism. Following Patrick et al. (2011), we consider that the transfer of a rockfall's momentum to the lava column during impact, likely induced a pressure transient that transmitted through the conduit and eventually reached the reservoir, causing the collapse of the larger gas pocket associated with the tremor lower frequency peak.

In analogy, at a larger scale, the first small collapse events that occurred during Phase 3, could have had a similar effect on the reservoir than the rockfall impacts on the lava surface. For example, after the first collapse on May 17, we observe the cessation of the frequency peak at ~0.7 Hz. With each collapse event, the gas on the top of the reservoir could go back into solution (e.g., Soubestre et al., 2021), re-compress, and/or escape to the surface, contributing to the explosions. The explosive activity in Phase 3 grew in intensity: in Phase 2 the explosion plumes attained ~2000 m of height, whereas in Phase 3 they reached ~8100 m (Neal et al., 2019). Additionally, summit SO_2 emission rates increased by two to three times and peaked during this stage of explosive activity (Kern et al., 2020), indicating a strong magmatic component. Thus, it can be interpreted that the gas at the top of the reservoir was forced to escape towards the surface under the influence of the collapses.

In Phase 4, even if the collapses became much larger (Anderson et al., 2019), the explosive activity ceased (Neal et al., 2019). Thus, we interpret that the gas content and the exsolution rate had decreased enough by then so that the impact of the collapses could not trigger the explosions anymore. This highlights the magma degassing as a necessary precondition for explosive activity.

5. Conclusions

We provided a new method for locating sources of tremor. The method relies on an amplitude decay model extracted from high-quality earthquake data using ML. To the best of our knowledge, this is the first time this methodology has been applied. We showed that our method is more accurate than the traditional amplitude source location method. This method can be applied at other instrumented volcanoes where a comprehensive seismic catalog has been recorded. This requirement is usually met at volcano observatories, where routine monitoring tasks include earthquake location.

We applied our method to the Kīlauea summit deflation tremor during the 2018 eruption and caldera collapse. Our results point to a source located ~1 km below the eastern perimeter of the Halema'uma'u crater. Based on this result, which coincides with other geophysical studies, we consider that the source of this tremor was located at the top of the shallow magma reservoir. Additionally, the correlation between reservoir decompression and tremor amplitude suggests that the tremor source was associated with volatile exsolution caused by magma depressurization.

We provided a tremor model in which the exsolved gas, after accumulating at the top of the reservoir in a series of gas pockets, flows through permeable rocks of the roof generating pressure oscillations. In our model, the multi-chromatic character of the signal is explained by a system of resonators, in which each resonator is responsible for a single major spectral peak. Fluctuations in the gas mass flux rate explain the tremor amplitude variations, whereas the thickness of the gas pockets controls the frequency gliding.

We complemented our results of seismic tremor with an analysis of the infrasound signal, to assess the connection between the processes at depth with the atmosphere. At the surface, the decompression-driven degassing manifested as infrasonic tremor, by generating a resonance at the void section of the Overlook vent. Additionally, we concluded that the explosions triggered by the impact of rock falls on the surface of the lava lake, likely influenced the processes taking place at the reservoir.

After a period of mostly steady subsidence, by recompressing the magma, the first small collapses periodically interrupted the generation of tremor, resulting in a cyclic character of its variations. Beyond a critical point, the relaxation of magma caused the cessation of tremor and explosive activity, while clearing the way for the large collapses to happen.

An important goal of physical volcanology is to understand the mechanisms responsible for the monitoring signals observed during episodes of volcanic unrest. Therefore, we developed a novel tool for the location of the source of

volcanic tremor. Additionally, we provided a viable mechanism to explain the Kīlauea summit tremor during phases of deflation and eruptive activity. In the future, we will focus our research on applying our tremor location methods to other volcanoes with different network configurations and seismic catalogs; and applying our tremor inversion technique to other volcanic scenarios.

Author contributions

Acknowledgments

Data availability

All seismic and infrasound data used in this paper comes from the Incorporated Research Institutions for Seismology (IRIS) Data Management Center. Tilt data comes from Johanson and Miklius (2019). Lava lake elevation data comes from Patrick et al. (2022). Earthquake catalog from the caldera collapse comes from Shelly and Thelen (2019). The code for tremor location can be found at github.com/lvanderlaat/tl.git. The code for tremor inversion can be found at github.com/lvanderlaat/ti.git. The code used for the LTS analysis was obtained at github.com/uafgeotools/lts_array.

Appendix A. Machine-learning amplitude source location

Appendix A.1. Feature extraction, engineering, and selection

We extracted the RMS of the seismic amplitudes recorded in the seismic stations shown in Figure 1a. We assumed that the waves from earthquakes and tremor share the same amplitude decay. Theoretically, this depends on the type of wave (body or shallow). We took the whole waveform of the earthquake, including P, S, and surface waves in order to approximate a general amplitude decay function during the learning stage. For earthquakes, we used a 20-second window from the origin time. For tremor, we used a 15-minute moving window with 50% overlap to avoid the influence of discrete earthquakes. We first remove the trend and instrument response and decimate the signal by a factor of 2 to obtain a 50 Hz sampling rate. Then, we filtered the signal in 4 narrow frequency bands (0.38-1.2 Hz, 1.2-2.3 Hz, 2.3-3.4 Hz, and 3.4-4.5 Hz) using an order 2 Butterworth filter. We recorded one RMS amplitude value for each frequency band and in each channel of the network. The selected frequency range (0.38-4.5 Hz) corresponds to the overlapping band between earthquakes and tremor (Supplementary Fig. S5). The lower frequency cut-off allowed to filter out the microseism bands (Supplementary Fig. S5).

In the traditional ASL method, it is advised to compute the amplitude ratios between all pairs of stations, since this procedure removes the influence of the source amplitude A_0 (Taisne et al., 2011). Also, the amplitude ratios provide more information about how the amplitude is distributed in the network to the model. Thus, we computed the ratios of the RMS amplitudes measured in the same frequency band for all pairs of channels of the same component (east, north, or vertical).

Then, we computed three transformations of the amplitude ratios: the square root, the natural logarithm, and the real part of the Lambert W function. These transformations were selected based on the physical knowledge. When solving Equation 1 for the source-receiver distance d_i, we observe that d_i is dependent of the real part of the Lambert W function and the natural logarithm of the amplitude:

$$d_i(A_i) = \frac{\alpha}{B} \mathrm{Re}\left[W\left(\frac{B}{\alpha} \exp\left(\frac{\ln(A_0/A_i)}{\alpha} \right) \right) \right] \tag{A.1}$$

The square root was selected via experimentation since it yielded positive results.

In order to select the best set of features, we trained and tested several models with all possible combinations of the transformations, including the unaltered amplitude ratio. Then, we selected the combination of transformations that yielded the lower test errors. This selection process allowed to simplify the model, decrease the computation time and increase the quality of the model.

Appendix A.2. Model training and testing

The data set for training and testing corresponds to the earthquake catalog from Shelly and Thelen (2019). During training, we only considered events with magnitudes between 1.1 and 4. This is the magnitude range where the Gutenberg-Richter Law was best fitted (Supplementary Fig. S6). Below the lower cutoff magnitude value we expect a decrease in the level of detection, i.e. we would observe lower signal-to-noise ratios (SNR). Using low SNR data could diminish the performance of our model. The filtered catalog contained 22,719 events. We divided the data set as follows: 70% (15,904 events) for training, and 30% (6,815 events) for testing.

The models were trained using linear least squares with L2 regularization, a.k.a. ridge regression. This algorithm minimizes the objective function:

$$L = \left(\|Y - Xw\|_2^2 + \alpha\|w\|_2^2 \right) \tag{A.2}$$

where, X is the feature matrix, Y is the target vector, w is the vector of coefficients of the model, and the hyper-parameter α controls the severity of the regularization. With a high α, a model becomes more robust to co-linearity. In order to estimate the best α, we used the leave-one-out (LOO) cross-validation with $\alpha \in \{1, 10^1, 10^2, 10^3, 10^4\}$.

The L2 regularizer assumes that all features are centered around 0 and vary in the same order of magnitude. Thus, we standardized the training, test, and new predictions data sets. First, we computed the training data set features means, and variances. Then, for each data set, we removed the mean and divided by the variance.

The test error was defined as the Euclidean distance, in meters, between the true and the predicted locations of the test set. We also computed the error in each of the Cartesian coordinates independently, in order to determine if there was any spatial bias in the model. Lastly, the final model for tremor location was trained with the whole data set. We also computed the "total error", which corresponds to the mean misfit of the final model for all events, both in the training and test sets. For data standardization, training, and cross-validation we used the SciKit-Learn Python package Pedregosa et al. (2011).

Appendix A.3. Synthetic tests

In order to validate our method and obtain a measure of uncertainty, we trained a model with synthetic amplitude data. We took the catalog of events and computed synthetic amplitude data for each receiver using the attenuation model (Equation 1), with d_i as imposed by the catalog locations, $Q = 50$, $f = 2$ Hz, $c = 2309$ m/s and $\alpha = 0.5$. For the source amplitude A_0 we assigned the exponent of the magnitude. Then, we engineered the features and trained a model as previously described. After that, for each point in a 3-dimensional grid, we simulated the expected amplitudes in the seismic network. The grid covers the area of the seismic network (Figure 1) and extends down to 10 km deep. We used a 100-m spacing between consecutive points. We located each source with the model trained on synthetic amplitude data and computed the misfits.

Appendix A.4. Traditional amplitude source location

In order to estimate the performance of our method, we compare the results to those of the traditional ASL method. For this method, it is required to correct site amplification effects. To determine the correction factors we follow a similar methodology to that applied by Eibl et al. (2017). We used the catalog from (Shelly and Thelen, 2019). The RMS amplitudes (3.4-4.5 Hz) were normalized and sorted with respect to the hypocentral distance. We took the median amplitude in a 100 m-window along the source-receiver distance in order to decrease the dispersion of the data. The data distribution was then fitted with the attenuation model (Equation 1) using non-linear least squares optimization (Supplementary Fig. S12). The parameters of the model were allowed to vary as follows: $Q_f \in 1 - 200$, $A_0 > 1$ and $c \in 1500 - 3500$ m/s. We fixed $\alpha = 1$ and $f = 4$ Hz. Finally, we calculated the site correction factors for each station by dividing the observed amplitudes by the amplitude expected from the best-fit model (Supplementary Table S1).

In order to directly compare the results of the ASL and ML-ASL methods we used the ASL method to relocate the test set used during the learning stage of the ML-ASL model. The location method was implemented as done by Taisne et al. (2011). We used a rectangular grid with a spacing of 100 m between consecutive points. The grid comprises an area determined by the minimum and maximum latitudes and longitudes in the seismic network and extends vertically from 0.8 km above sea level down to 3.5 km below sea level.

Appendix B. Tremor model

Appendix B.1. Inversion method

For the tremor inversion, the seismic records from the vertical component were pre-processed as follows. First, we detrended, filtered between 0.38 and 6.2 Hz (to avoid long-period oceanic noise contamination), decimated to a 12.5 Hz sampling rate, and corrected the instrument response of the data. We divided the data into 1-hour windows and 120 30-s sub-windows. For each sub-window, we computed the fast Fourier transform (FFT) amplitude spectrum and then took the 1-hour median spectrum over the sub-windows.

We generated synthetic velocity seismograms using the forward model from Girona et al. (2019). Since this tremor is multichromatic, we consider that each spectral peak corresponds to a single resonator. Together, many resonators in a system generate the resulting multichromatic tremor. Although, the studied tremor signal shows many spectral peaks, the number of the most prominent is less than five. Thus, in order to reduce the model complexity, we fix the maximum number of sub-resonators to be simulated to 5.

Before computing the misfit, both observed and synthetic spectra were smoothed with a Gaussian filter with a standard deviation for the Gaussian kernel equal to 1. The misfit (χ) between the observed spectrum (**p**) and synthetic spectrum (**q**) was calculated as:

$$\chi(\mathbf{p}, \mathbf{q}) = \sqrt{(d \cos a)^2 + (d \sin a)^2} \tag{B.1}$$

with d, the Euclidean distance between the spectra:

$$d(\mathbf{p}, \mathbf{q}) = \sqrt{\sum_{i=1}^{N} (p_i - q_i)^2} \tag{B.2}$$

and a, the spectral angle:

$$a(\mathbf{p}, \mathbf{q}) = \cos^{-1} \left(\frac{\sum_{i=1}^{N} p_i q_i}{\sqrt{\sum_{i=1}^{N} (p_i)^2} \sqrt{\sum_{i=1}^{N} (q_i)^2}} \right) \tag{B.3}$$

N is the number of samples in the spectra. The spectral angle a provides a measure of the similarity of the shape between the spectra regardless of their absolute amplitudes. Weighting a with d (Equation B.1) ensures fitting both amplitude and frequency distribution.

The potential solutions of the inversion were constrained by restricting the natural frequency of the resonators to a narrow range (±0.025 Hz) around the frequencies of the most prominent peaks. The prominence of a peak is defined

as the normalized vertical distance between the peak and its lowest contour line. We only considered peaks with a prominence larger than 0.2.

For the inversion, we used the implementation of Blank and Deb (2020) of the genetic algorithm. We started with a population of 100 individuals and iterated through 300 generations. At the end of each iteration, we selected the best individuals to be the new parents using the tournament selection. Then we generated a new offspring population of 30 individuals through simulated binary crossover (SBX) and mutated them using polynomial mutation. Since no solution is known *a priori*, and in order to maintain the diversity, we set the SBX and mutation parameters to 1.

In order to obtain the uncertainty of the model, we repeated the experiment 1000 times, then averaged the results. We utilized the standard deviation derived from multiple evaluations to determine the performance and reliability of the model.

Appendix B.2. Model parameters

We allowed the mean gas flux (Q_0) and thickness of the gas pocket (D) to vary, while the rest of the parameters were fixed. The quality factor of the wave propagation medium was chosen ($Q_f = 50$) based on Koyanagi et al. (1995) and the density of the medium was fixed to a typical value for basaltic rocks ($\rho_s = 2800$ kg/m^3). We fixed the source position based on our tremor location results Table B.1. We assumed a CO_2-rich magma composition with 0.3 wt% H_2O and 0.65 wt% CO_2 (Gerlach and Graeber, 1985), which yields a molecular weight of 36 g/mol.

Table B.1: Tremor simulation parameters

Parameter	Description	Value	Unit
τ	Duration of the synthetic seismogram	30	s
x	Cartesian easting	712	m
y	Cartesian northing	250	m
z	Elevation	300	m a.s.l.
μ_g	Gas viscosity	1×10^{-5}	Pa $\cdot$ s
T	Gas temperature	1,273	K
M	Gas molecular weight	0.036	kg/mol
R_g	Ideal gas constant	8.3145	J/K/mol
N	Number of impulses	60	per minute
Q_0	Mean gas flux	[0.1 — 3,000]	kg/s
R	Resonator radius	40	m
D	Gas pocket thickness	[0.0 — 4.0]	m
L	Cap thickness	30	m
κ	Cap permeability	1×10^{-10}	m^2
φ	Cap porosity	0.01	%
P_{ex}	External pressure	21.9	MPa
ρ_s	Medium density	2,800	kg/m^3
Q_f	Quality factor	50	

The resonators share a common permeable cap with effective thickness L (Figure 6b), which could correspond to the thermal boundary layer surrounding the magma body. For simplicity, since the thickness D of the gas pocket is much smaller than L (around 1 to 3 orders of magnitude), we consider a constant L for all resonators. From our tremor location, and the reservoir model from Anderson et al. (2019), this cap is buried at a depth of ~800 m. With a rock density ρ_s of 2800 kg/m^3, the external pressure at the top of the cap, is around $P_{ex} = 21.95$ MPa. For L in the order of a few meters to tens of meters, the pressure drop along the cap is small compared to P_{ex} (~3%), which is a necessary condition to obtain the approximated analytical equation in Girona et al. (2019).

In order to constrain the values of the permeable cap parameters properties, we first investigated the effect of the parameters on the natural frequency f_{nat} of the resonator. We computed f_{nat} using equation 26 in Girona et al. (2019) for different values of the cap properties (thickness L, permeability κ and porosity φ), and varying values of D (Supplementary Fig. S14). In order to obtain values of f_{nat} in the range of the observed tremor (0.3 - 4 Hz), it was

determined that L must be in the range between 5 and 30 m (Supplementary Fig. S14), and φ between 0.01 and 0.1%. These results are similar for different values of the mean gas flux Q_0 (1 - 700 kg/s, Supplementary Fig. S14).

Additionally, we inverted several models for different values of the parameters investigated (Supplementary Fig. S15, Supplementary Fig. S16). Very thin permeable caps ($L \leq 15$ m), or a cap porosity of 0.1 % yield values of gas mean flux Q_0 which are significantly larger than the expected gas flux from the reservoir decompression (Appendix Appendix C, Supplementary Fig. S19). The permeability κ has no significant effect on the models (Supplementary Fig. S15b and Supplementary Fig. S16b). Based on these results, we fixed these parameters as shown in Table B.1.

Appendix C. Gas flux determination based on the reservoir decompression

During Phase 2, radial tilt was directly correlated to the magma reservoir pressure (Anderson et al., 2019). We used the scaling factor at station UWD (0.078 ± 0.006 MPa per microradian of radial tilt) established by Anderson et al. (2019) to obtain the reservoir pressure time series (Figure 8a). Tilt data came from Johanson and Miklius (2019). We considered data from the start of the deflation on May 1st, 2018, to the first collapse on May 17, 2018. After that date, the compression induced by the collapses complicates the analysis since the amount of resorption that occurred is unknown.

First, we rotated the north and east components to obtain the radial component with respect to the source of deformation, i.e., the reservoir, at a backazimuth of 136°. Then, we corrected the tectonic offset caused by the M 6.9 detachment earthquake on May 5. After scaling tilt to obtain pressure, assuming an initial pressure of 45 MPa (Anderson et al., 2019), we downsampled the time series from 1-minute to 1-hour period and smoothed the data by taking the median in a centered 1-day-long moving window (red line in Figure 8a).

Next, considering the pressure variation and a typical basaltic magma composition with 50.3 wt% SiO_2 (Thornber et al., 2003), we calculated the degassing path using the exsolution model of Dixon (1997) as implemented by Iacovino et al. (2021) following Newman and Lowenstern (2002). In the open-system degassing model, the magma is depressurized along a series of steps. At each step, the melt composition and vapor compositions are re-calculated until they are in equilibrium with the vapor exsolved during that step (Newman and Lowenstern, 2002).

With regards to the volatile budget of the starting magma composition, we considered two end-member scenarios based on Gerlach and Graeber (1985) modeling for the Kīlauea summit reservoir: a CO_2-rich magma with 0.3 wt% H_2O and 0.65 wt% CO_2 and CO_2-poor magma with 0.27 wt% H_2O and 0.02 wt% CO_2 (Supplementary Fig. S19). The variation between these two compositions depends on the amount of exsolution that occurred in the reservoir since the time of supply (Gerlach and Graeber, 1985; Gerlach, 1986).

The fluid proportion was converted to mass by multiplying by ρ and V. Those values were taken from Anderson and Poland (2016) and Anderson et al. (2019), respectively. We consider two end-member scenarios based on the range of the estimates: 1. $\rho = 2550$ kg/m^3 and $V = 2.5$ km^3, and; 2. $\rho = 2650$ kg/m^3 and $V = 7.2$ km^3. Finally, the gas flux rate Q^D was obtained by differentiating the mass with respect to time.

Appendix D. Infrasonic tremor

Appendix D.1. Detection

We analyzed data from the array of infrasound sensors NPT (Figure 1). The available time period for this data, May 4-25, 2018, covers most of Phases 2 and 3 (Figure 2). To increase the signal-to-noise ratio of the infrasound records we used two techniques. First, we estimated the magnitude squared coherence (C_{xy}) between sensors 1 and 2 of the array, which are 52 m apart. For two discrete-time signals x and y, the coherence is defined as:

$$C_{xy}(f) = \frac{\left|(S_{xy}(f))\right|^2}{S_{xx}(f)\, S_{yy}(f)} \tag{D.1}$$

where $S_{xx}(f)$ and $S_{yy}(f)$ are the power spectral density estimates of x and y, respectively, and $S_{xy}(f)$ is the cross-spectral density estimate of the two signals (Welch, 1967). We computed C_{xy} for every 1-hour window, and downsampled the data by taking the mean of each 0.01 Hz bin between 0.01 and 8 Hz.

Secondly, we used the least trimmed squares (LTS) algorithm, which computes the cross-correlation function and lag times between all pairs of sensors (Bishop et al., 2020). The main purpose of the LTS algorithm is to determine the sound velocity and backazimuth of the source of the infrasonic signal. In this algorithm, the median of the cross-correlation maxima is used as a coherence metric of the potential signal. In our processing, we first filtered the signal between 0.1 and 5 Hz, and then ran the LTS algorithm for a 30 s-moving window with 50% of overlap.

In order to further assess the correlation of the activity at the Overlook vent with the infrasound data, we synchronized the LTS results with the time-lapse movie of the thermal camera (Anderson et al., 2019); the sped-up sound reproduction of the beamformed infrasound recordings; and the relative seismic and infrasound amplitude measurements. The beamformed infrasound data was obtained by stacking the traces from all sensors, after removing the travel-time differences, based on an assumed acoustic plane wave arriving from the Overlook vent.

We detected coherent infrasonic signals coming from the direction of the Overlook vent (Figure 1) ($\sim$180° backazimuth, Supplementary Fig. S20). Between May 5 and 8, the signal was weak and intermittent, with frequencies above 1 Hz (Supplementary Fig. S20a). Starting on May 7 at 11:00 (UTC), a weak low-frequency ($\sim$0.5 Hz) signal was detected. This signal gained strength by May 8 at 01:00 (UTC), and was characterized by a broadband spectral peak at $\sim$0.5 Hz and other higher frequency peaks (1-5 Hz, Supplementary Fig. S20b). On May 10, this signal disappeared suddenly.

The synchronization of the thermal camera images and the infrasound analysis results (Supplementary Movie S2) reveals that shorter signals detected between May 5 and 8 correspond to explosions, such as the one shown in Supplementary Fig. S20e. After an explosion on May 7 at 08:10 (UTC), the lava became profusely bubbly (Supplementary Fig. S20f). This type of degassing activity continued for the rest of the thermal camera recording, which ended on May 9 at 18:20 (UTC). This activity timely coincided with the detected continuous infrasonic tremor (May 7-11, Supplementary Movie S2).

Appendix D.2. Helmholtz resonance

The infrasonic tremor, detected between May 7 and 10, 2018 (Supplementary Fig. S20), coincided with a profuse bubbling activity in the lava lake (Supplementary Movie S2), which at that moment had drained significantly, leaving behind a void pipe of around 250 m in length (Supplementary Fig. S20a). Based on these observations and following Fee et al. (2010), we consider that the degassing at the lava surface established pressure oscillations at the pipe, generating a Helmholtz resonance (Figure 6a).

The Helmholtz resonator consists of a cavity with an opening or neck with length L. A typical example of a Helmholtz resonance is when air is blown into a bottle creating a tonal sound. In our magmatic vent case, as gas is being pushed out from the lava surface, the pressure in the cavity decreases. The pressure gradient causes a pull of the air in the neck (i.e., rim of the vent) back into the cavity, generating standing waves.

The frequency f of the Helmholtz resonance is given by:

$$f = \frac{c}{2\pi} \sqrt{\frac{S_n}{VL'}}, \tag{D.2}$$

where c is the speed of sound, S_n is the surface area of the resonator neck, V is the volume of the resonator cavity, and $L' = L + \Delta L$ is the effective length of the neck, which accounts for the extra volume of air that is displaced in the neck. A correction factor c_f to obtain the effective length, depends on the geometry of the resonator, specifically the ratio ξ between the section plane of the neck (S_n) and the section plane of cavity (S_c), $\xi = S_n/S_c$ (Catapane et al., 2022). The effective length is given by $L' = L(1 + c_f\xi)$.

Furthermore, the quality factor of the resonance Q is given by:

$$Q = 2\pi \sqrt{V\left(\frac{L'}{S_n}\right)^3}. \tag{D.3}$$

The volume of the cavity (i.e., the pipe) can be realistically approximated as a cylinder ($V = \pi r_c^2 h$), with radius r_c and height h. Equation D.2 and Equation D.3 then become:

$$f = \frac{c}{2} \sqrt{\frac{S_n}{\pi^3 r_c^2 h L'}}, \tag{D.4}$$

and:

$$Q = 2\sqrt{\pi^3 r_c^2 h \left(\frac{L'}{S_n}\right)^3}. \tag{D.5}$$

We solved Equation D.4 and Equation D.5 together for the cavity radius r_c and the equivalent length of the neck L'. The other parameters (f, Q, S_n, c, h) were estimated as described in Table D.2. We measured f and Q in a 5-minute moving window with a 30 s-step and obtained r_c and L' for each window.

Table D.2: Helmholtz resonator model parameters

Parameter	Value	Reference/Determination
f	0.47 ± 0.053 Hz	From the infrasound records. Center frequency of the lowest and most prominent spectral peak (median ± standard deviation).
Q	1.02 ± 0.25	From the infrasound records, ratio of the center frequency to the frequency band where the energy reaches half of its value (median ± standard deviation).
S_n	$\pi \times 125\,\text{m} \times 90\,\text{m}$	As an ellipse, from visual observation of satellite image.
c	$468\,\text{m s}^{-1}$	For a gas mixture at ~200°C (Kumagai and Chouet, 2000)
h	290-360 m	Linear increase of empty section of the pipe from the lake elevation data (Patrick et al., 2022).

Our modeling yielded $L' = 37 \pm 7$ m and $r_c = 154 \pm 24$ m. Although the actual length L of the neck depends on an unknown correction factor, its upper limit is defined by the effective length (i.e. $L < 37$ m). Our estimated r_c is consistent with the three-dimensional photogrammetric model of the crater by Patrick et al. (2022). The expected change of frequency from the cavity growth, due to the drainage of the lava, is not significant ($0.5 - 0.45$ Hz = 0.05 Hz), and it would be difficult to observe since the width of the peak (0.46 ± 0.122 Hz) is much larger (Supplementary Fig. S20a). The lower-amplitude, higher-frequency peaks could be modeled following Fee et al. (2010), but it is out of the scope of this work.

Appendix E. Supplementary data

Supplementary data to this article can be found online at https://www.overleaf.com/3141127523ymfrnvdmfjph

References

Almendros, J., Chouet, B., Dawson, P., 2001. Spatial extent of a hydrothermal system at Kilauea Volcano, Hawaii, determined from array analyses of shallow long-period seismicity 2. Results. Journal of Geophysical Research: Solid Earth 106. doi:10.1029/2001jb000309.

Anderson, K., Johanson, I., 2022. Incremental caldera collapse at Kīlauea Volcano recorded in ground tilt and high-rate GNSS data, with implications for collapse dynamics and the magma system. Bulletin of Volcanology 84, 89. URL: https://doi.org/10.1007/s00445-022-01589-x, doi:10.1007/s00445-022-01589-x.

Anderson, K.R., Johanson, I.A., Patrick, M.R., Gu, M., Segall, P., Poland, M.P., Montgomery-Brown, E.K., Miklius, A., 2019. Magma reservoir failure and the onset of caldera collapse at Kīlauea Volcano in 2018. Science 366. doi:10.1126/science.aaz1822.

Anderson, K.R., Poland, M.P., 2016. Bayesian estimation of magma supply, storage, and eruption rates using a multiphysical volcano model: Kīlauea Volcano, 2000–2012. Earth and Planetary Science Letters 447, 161–171. doi:10.1016/J.EPSL.2016.04.029.

Ardid, A., Dempsey, D., Caudron, C., Cronin, S., 2022. Seismic precursors to the Whakaari 2019 phreatic eruption are transferable to other eruptions and volcanoes. Nature Communications 13, 2002. URL: https://doi.org/10.1038/s41467-022-29681-y, doi:10.1038/s41467-022-29681-y.

Bagnardi, M., Poland, M.P., Carbone, D., Baker, S., Battaglia, M., Amelung, F., 2014. Gravity changes and deformation at Kīlauea Volcano, Hawaii, associated with summit eruptive activity. Journal of Geophysical Research: Solid Earth doi:10.1002/2014JB011506.

Baker, S., Amelung, F., 2012. Top-down inflation and deflation at the summit of Klauea Volcano, Hawaii observed with InSAR. Journal of Geophysical Research: Solid Earth 117. doi:10.1029/2011JB009123.

Ballmer, S., Wolfe, C.J., Okubo, P.G., Haney, M.M., Thurber, C.H., 2013. Ambient seismic noise interferometry in Hawai'i reveals long-range observability of volcanic tremor. Geophysical Journal International 194. doi:10.1093/gji/ggt112.

Battaglia, J., Aki, K., 2003. Location of seismic events and eruptive fissures on the Piton de la Fournaise volcano using seismic amplitudes. Journal of Geophysical Research 108, 3–14. doi:10.1029/2002jb002193.

Battaglia, J., Aki, K., Ferrazzini, V., 2005. Location of tremor sources and estimation of lava output using tremor source amplitude on the Piton de la Fournaise volcano: 1. Location of tremor sources. Journal of Volcanology and Geothermal Research 147, 268–290.

Beyreuther, M., Barsch, R., Krischer, L., Megies, T., Behr, Y., Wassermann, J., 2010. ObsPy: A python toolbox for seismology. Seismological Research Letters 81. doi:10.1785/gssrl.81.3.530.

Bishop, J.W., Fee, D., Szuberla, C.A., 2020. Improved infrasound array processing with robust estimators. Geophysical Journal International 221. doi:10.1093/GJI/GGAA110.

Blank, J., Deb, K., 2020. Pymoo: Multi-Objective Optimization in Python. IEEE Access 8. doi:10.1109/ACCESS.2020.2990567.

Catapane, G., Magliacano, D., Petrone, G., Casaburo, A., Franco, F., De Rosa, S., 2022. Semi-analytical estimation of Helmholtz resonators' tuning frequency for scalable neck-cavity geometric couplings. CEAS Aeronautical Journal 13, 797–808. URL: https://doi.org/10.1007/s13272-022-00592-4, doi:10.1007/s13272-022-00592-4.

Chouet, B., 1986. Dynamics of a fluid-driven crack in three dimensions by the finite difference method. Journal of Geophysical Research 91. doi:10.1029/jb091ib14p13967.

Chouet, B., Dawson, P., 2011. Shallow conduit system at Kilauea Volcano, Hawaii, revealed by seismic signals associated with degassing bursts. Journal of Geophysical Research: Solid Earth 116. doi:10.1029/2011JB008677.

Chouet, B., Dawson, P., 2013. Very long period conduit oscillations induced by rockfalls at Kilauea Volcano, Hawaii. Journal of Geophysical Research: Solid Earth 118. doi:10.1002/jgrb.50376.

Chouet, B.A., Dawson, P.B., James, M.R., Lane, S.J., 2010. Seismic source mechanism of degassing bursts at Kilauea Volcano, Hawaii: Results from waveform inversion in the 10-50 s band. Journal of Geophysical Research: Solid Earth 115. doi:10.1029/2009JB006661.

De la Cruz-Reyna, S., Reyes-Dávila, G.A., 2001. A model to describe precursory material-failure phenomena: Applications to short-term forecasting at Colima volcano, Mexico. Bulletin of Volcanology 63, 297–308. doi:10.1007/s004450100152.

Dempsey, D.E., Cronin, S.J., Mei, S., Kempa-Liehr, A.W., 2020. Automatic precursor recognition and real-time forecasting of sudden explosive volcanic eruptions at Whakaari, New Zealand. Nature Communications 11. doi:10.1038/s41467-020-17375-2.

Dixon, J.E., 1997. Degassing of alkalic basalts. American Mineralogist 82. doi:10.2138/am-1997-3-415.

Donaldson, C., Caudron, C., Green, R.G., Thelen, W.A., White, R.S., 2017. Relative seismic velocity variations correlate with deformation at Kīlauea volcano. Science Advances 3. doi:10.1126/sciadv.1700219.

Eibl, E.P., Bean, C.J., Vogfjörd, K.S., Ying, Y., Lokmer, I., Möllhoo, M., O, G.S., Pálsson, F., 2017. Tremor-rich shallow dyke formation followed by silent magma flow at Bardarbunga in Iceland. Nature Geoscience 10. URL: www.nature.com/naturegeoscience, doi:10.1038/NGEO2906.

Fee, D., Garcés, M., Patrick, M., Chouet, B.A., Dawson, P., Swanson, D., 2010. Infrasonic harmonic tremor and degassing bursts from Halema'uma'u Crater, Kilauea Volcano, Hawaii. Journal of Geophysical Research: Solid Earth 115. doi:10.1029/2010JB007642.

Gerlach, T., 1986. Exsolution of H20 , CO2, and S during eruptive episodes. Journal of Geophysical Research: Solid Earth 91.

Gerlach, T.M., Graeber, E.J., 1985. Volatile budget of Kilauea volcano. Nature 313. doi:10.1038/313273a0.

Girona, T., Caudron, C., Huber, C., 2019. Origin of Shallow Volcanic Tremor: The Dynamics of Gas Pockets Trapped Beneath Thin Permeable Media. Journal of Geophysical Research: Solid Earth doi:10.1029/2019JB017482.

Hotovec-Ellis, A.J., Shiro, B.R., Shelly, D.R., Anderson, K.R., Haney, M.M., Thelen, W.A., Montgomery-Brown, E.K., Johanson, I.A., 2022. Earthquake-Derived Seismic Velocity Changes During the 2018 Caldera Collapse of Kīlauea Volcano. Journal of Geophysical Research: Solid Earth 127, e2021JB023324. URL: https://agupubs.onlinelibrary.wiley.com/doi/abs/10.1029/2021JB023324, doi:https://doi.org/10.1029/2021JB023324.

Iacovino, K., Matthews, S., Wieser, P.E., Moore, G.M., Bégué, F., 2021. VESIcal Part I: An Open-Source Thermodynamic Model Engine for Mixed Volatile (H2O-CO2) Solubility in Silicate Melts. Earth and Space Science 8. doi:10.1029/2020EA001584.

Ichihara, M., Matsumoto, S., 2017. Relative Source Locations of Continuous Tremor Before and After the Subplinian Events at Shinmoe-dake, in 2011. Geophysical Research Letters 44, 871–10. doi:10.1002/2017GL075293.

Jaupart, C., Vergniolle, S., 1989. The Generation and Collapse of a foam Layer at the Roof of a Basaltic Magma Chamber. Journal of Fluid Mechanics 203. doi:10.1017/S0022112089001497.

Johanson, I., Miklius, A., 2019. Tiltmeter data from Kīlauea Volcano, Hawaii, spanning the 2018 eruption and earthquake sequence.

Johnson, D.J., 1992. Dynamics of magma storage in the summit reservoir of Kilauea volcano, Hawaii. Journal of Geophysical Research 97. doi:10.1029/91JB02839.

Jolly, A.D., Thompson, G., Norton, G.E., 2002. Locating pyroclastic flows on Soufriere Hills Volcano, Montserrat, West Indies, using amplitude signals from high dynamic range instruments. Journal of Volcanology and Geothermal Research 118, 299–317. doi:10.1016/S0377-0273(02)00299-8.

Jones, J., Carniel, R., Harris, A.J., Malone, S., 2006. Seismic characteristics of variable convection at Erta 'Ale lava lake, Ethiopia. Journal of Volcanology and Geothermal Research 153, 64–79. doi:10.1016/j.jvolgeores.2005.08.004.

Julian, B.R., 1994. Volcanic tremor: nonlinear excitation by fluid flow. Journal of Geophysical Research 99. doi:10.1029/93jb03129.

Kern, C., Lerner, A.H., Elias, T., Nadeau, P.A., Holland, L., Kelly, P.J., Werner, C.A., Clor, L.E., Cappos, M., 2020. Quantifying gas emissions associated with the 2018 rift eruption of Kīlauea Volcano using ground-based DOAS measurements. Bulletin of Volcanology 82. doi:10.1007/s00445-020-01390-8.

Koyanagi, S., Aki, K., Biswas, N., Mayeda, K., 1995. Inferred attenuation from site effect-corrected T phases recorded on the island of Hawaii. Pure and Applied Geophysics PAGEOPH 144, 1–17. doi:10.1007/BF00876471.

Kumagai, H., Chouet, B.A., 2000. Acoustic properties of a crack containing magmatic or hydrothermal fluids. Journal of Geophysical Research: Solid Earth 105, 25493–25512. doi:10.1029/2000jb900273.

Kumagai, H., Palacios, P., Maeda, T., Castillo, D.B., Nakano, M., 2009. Seismic tracking of lahars using tremor signals. Journal of Volcanology and Geothermal Research doi:10.1016/j.jvolgeores.2009.03.010.

van der Laat, L., Mora, M.M., Pacheco, J.F., Lesage, P., Meneses, E., 2022. Seismicity during the recent activity (2009–2020) of Turrialba volcano, Costa Rica. Journal of Volcanology and Geothermal Research 431, 107651–107651. doi:10.1016/J.JVOLGEORES.2022.107651.

Lengliné, O., Duputel, Z., Okubo, P.G., 2021. Tracking dike propagation leading to the 2018 Kīlauea eruption. Earth and Planetary Science Letters 553. doi:10.1016/j.epsl.2020.116653.

Lesage, P., Mora, M.M., Alvarado, G.E., Pacheco, J., Métaxian, J.P., 2006. Complex behavior and source model of the tremor at Arenal volcano, Costa Rica. Journal of Volcanology and Geothermal Research 157, 49–59. doi:`10.1016/j.jvolgeores.2006.03.047`.

Liang, C., Crozier, J., Karlstrom, L., Dunham, E.M., 2020. Magma Oscillations in a Conduit-Reservoir System, Application to Very Long Period (VLP) Seismicity at Basaltic Volcanoes: 2. Data Inversion and Interpretation at Kīlauea Volcano. Journal of Geophysical Research: Solid Earth 125. doi:`10.1029/2019JB017456`.

Liang, C., Dunham, E.M., 2020. Lava lake sloshing modes during the 2018 Kīlauea Volcano eruption probe magma reservoir storativity. Earth and Planetary Science Letters 535. doi:`10.1016/j.epsl.2020.116110`.

Macdonald, G.A., Eaton, J.P., 1964. Hawaiian volcanoes during 1955. U.S. Geological Survey Bulletin 1171 .

Neal, C.A., Brantley, S.R., Antolik, L., Babb, J.L., Burgess, M., Calles, K., Cappos, M., Chang, J.C., Conway, S., Desmither, L., Dotray, P., Elias, T., Fukunaga, P., Fuke, S., Johanson, I.A., Kamibayashi, K., Kauahikaua, J., Lee, R.L., Pekalib, S., Miklius, A., Million, W., Moniz, C.J., Nadeau, P.A., Okubo, P., Parcheta, C., Patrick, M.R., Shiro, B., Swanson, D.A., Tollett, W., Trusdell, F., Younger, E.F., Zoeller, M.H., Montgomery-Brown, E.K., Anderson, K.R., Poland, M.P., Ball, J.L., Bard, J., Coombs, M., Dietterich, H.R., Kern, C., Thelen, W.A., Cervelli, P.F., Orr, T., Houghton, B.F., Gansecki, C., Hazlett, R., Lundgren, P., Diefenbach, A.K., Lerner, A.H., Waite, G., Kelly, P., Clor, L., Werner, C., Mulliken, K., Fisher, G., Damby, D., 2019. The 2018 rift eruption and summit collapse of Kilauea Volcano. Science 363. doi:`10.1126/science.aav7046`.

Newman, S., Lowenstern, J.B., 2002. VOLATILECALC: A silicate melt-H2O-CO2 solution model written in Visual Basic for excel. Computers and Geosciences 28. doi:`10.1016/S0098-3004(01)00081-4`.

Orr, T.R., Thelen, W.A., Patrick, M.R., Swanson, D.A., Wilson, D.C., 2013. Explosive eruptions triggered by rockfalls at Kīlauea volcano, Hawai'i. Geology 41. doi:`10.1130/G33564.1`.

Patrick, M., Swanson, D., Orr, T., Younger, F., Tollett, W., 2022. Elevation of the lava lake in Halema'umaú crater, Kilauea Volcano, from 2009 to 2018. Technical Report. USGS.

Patrick, M., Wilson, D., Fee, D., Orr, T., Swanson, D., 2011. Shallow degassing events as a trigger for very-long-period seismicity at Kīlauea Volcano, Hawai'i. Bulletin of Volcanology 73. doi:`10.1007/s00445-011-0475-y`.

Patrick, M.R., Anderson, K.R., Poland, M.P., Orr, T.R., Swanson, D.A., 2015. Lava lake level as a gauge of magma reservoir pressure and eruptive hazard. Geology 43. doi:`10.1130/G36896.1`.

Patrick, M.R., Houghton, B.F., Anderson, K.R., Poland, M.P., Montgomery-Brown, E., Johanson, I., Thelen, W., Elias, T., 2020. The cascading origin of the 2018 Kīlauea eruption and implications for future forecasting. Nature Communications 11. doi:`10.1038/s41467-020-19190-1`.

Patrick, M.R., Orr, T., Sutton, A.J., Lev, E., Thelen, W., Fee, D., 2016. Shallowly driven fluctuations in lava lake outgassing (gas pistoning), Kilauea Volcano. Earth and Planetary Science Letters 433. doi:`10.1016/j.epsl.2015.10.052`.

Patrick, M.R., Younger, E.F., Tollett, W.D., 2019. Lava level and crater geometry data during the 2018 lava lake draining at Kīlauea Volcano, Hawaii. Technical Report. USGS. Hawaii. URL: `https://www.sciencebase.gov/catalog/item/5d842627e4b0c4f70d071a23`, doi:`10.5066/P9MJY24N`.

Pedregosa, F., Varoquaux, G., Gramfort, A., Michel, V., Thirion, B., Grisel, O., Blondel, M., Prettenhofer, P., Weiss, R., Dubourg, V., Vanderplas, J., Passos, A., Cournapeau, D., Brucher, M., Perrot, M., Duchesnay, E., 2011. Scikit-learn: Machine learning in Python. Journal of Machine Learning Research 12.

Poland, M.P., Jeff Sutton, A., Gerlach, T.M., 2009. Magma degassing triggered by static decompression at Kīlauea Volcano, Hawai'i. Geophysical Research Letters 36. doi:`10.1029/2009GL039214`.

Roman, D.C., Cashman, K.V., 2006. The origin of volcano-tectonic earthquake swarms. Geology 34. doi:`10.1130/G22269.1`.

Schlindwein, V., Wassermann, J., Scherbaum, F., 1995. Spectral analysis of harmonic tremor signals at Mt. Semeru Volcano, Indonesia. Geophysical Research Letters 22, 1685–1688. doi:`10.1029/95GL01433`.

Seydoux, L., Shapiro, N.M., De Rosny, J., Brenguier, F., Landès, M., 2016. Detecting seismic activity with a covariance matrix analysis of data recorded on seismic arrays. Geophysical Journal International doi:`10.1093/gji/ggv531`.

Shelly, D.R., Thelen, W.A., 2019. Anatomy of a Caldera Collapse: Kīlauea 2018 Summit Seismicity Sequence in High Resolution. Geophysical Research Letters 46. doi:`10.1029/2019GL085636`.

Soubestre, J., Chouet, B., Dawson, P., 2021. Sources of Volcanic Tremor Associated With the Summit Caldera Collapse During the 2018 East Rift Eruption of Kīlauea Volcano, Hawai'i. Journal of Geophysical Research: Solid Earth 126. doi:`10.1029/2020JB021572`.

Soubestre, J., Seydoux, L., Shapiro, N.M., de Rosny, J., Droznin, D.V., Droznina, S.Y., Senyukov, S.L., Gordeev, E.I., 2019. Depth Migration of Seismovolcanic Tremor Sources Below the Klyuchevskoy Volcanic Group (Kamchatka) Determined From a Network-Based Analysis. Geophysical Research Letters 46, 8018–8030. doi:`10.1029/2019GL083465`.

Taisne, B., Brenguier, F., Shapiro, N.M., Ferrazzini, V., 2011. Imaging the dynamics of magma propagation using radiated seismic intensity. Geophysical Research Letters 38. doi:`10.1029/2010GL046068`.

Thornber, C.R., Hon, K., Heliker, C., Sherrod, D.A., 2003. A compilation of whole-rock and glass major-element geochemistry of Kīlauea Volcano, Hawaii, near-vent eruptive products: January 1983 through September 2001. Open File Report 03-477 .

Unglert, K., Jellinek, A.M., 2015. Volcanic tremor and frequency gliding during dike intrusions at Kīlauea-A tale of three eruptions. Journal of Geophysical Research: Solid Earth 120, 1142–1158. doi:`10.1002/2014JB011596`.

U.S. Geological Survey, 2017. 1/3rd arc-second Digital Elevation Models (DEMs) - USGS National Map 3DEP Downloadable Data Collection.

Vergniolle, S., Jaupart, C., 1990. Dynamics of degassing at Kilauea Volcano, Hawaii. Journal of Geophysical Research 95. doi:`10.1029/JB095iB03p02793`.

Walsh, B., Jolly, A.D., Procter, J., 2017. Calibrating the amplitude source location (ASL) method by using active seismic sources: An example from Te Maari volcano, Tongariro National Park, New Zealand. Geophysical Research Letters 44, 3591–3599. doi:`10.1002/2017GL073000`.

Wang, T., Zheng, Y., Pulvirenti, F., Segall, P., 2021. Post-2018 Caldera Collapse Re-Inflation Uniquely Constrains Kīlauea's Magmatic System. Journal of Geophysical Research: Solid Earth 126. doi:`10.1029/2021JB021803`.

Welch, P., 1967. The use of fast Fourier transform for the estimation of power spectra: A method based on time averaging over short, modified periodograms. IEEE Transactions on Audio and Electroacoustics 15, 70–73. URL: `http://ieeexplore.ieee.org/document/1161901/`, doi:`10.1109/TAU.1967.1161901`.

White, R., McCausland, W., 2016. Volcano-tectonic earthquakes: A new tool for estimating intrusive volumes and forecasting eruptions. Journal

of Volcanology and Geothermal Research 309, 139–155. doi:10.1016/j.jvolgeores.2015.10.020.